A Probabilistic Neuro-symbolic Layer for Algebraic Constraint Satisfaction

Leander Kurscheidt[1] **Paolo Morettin**[2] **Roberto Sebastiani**[2] **Andrea Passerini**[2] **Antonio Vergari**[1]

[1]School of Informatics, University of Edinburgh, UK
[2]DiSI, University of Trento, Italy

Abstract

In safety-critical applications, guaranteeing the satisfaction of constraints over continuous environments is crucial, e.g., an autonomous agent should never crash into obstacles or go off-road. Neural models struggle in the presence of these constraints, especially when they involve intricate algebraic relationships. To address this, we introduce a differentiable probabilistic layer that guarantees the satisfaction of non-convex algebraic constraints over continuous variables. This probabilistic algebraic layer (PAL) can be seamlessly plugged into any neural architecture and trained via maximum likelihood without requiring approximations. PAL defines a distribution over conjunctions and disjunctions of linear inequalities, parameterized by polynomials. This formulation enables efficient and exact renormalization via symbolic integration, which can be amortized across different data points and easily parallelized on a GPU. We showcase PAL and our integration scheme on benchmarks for algebraic constraint integration and on real-world trajectory data.

1 INTRODUCTION

In safety-critical applications, a *reliable* AI system should be uncertainty-aware and deliver calibrated *probabilities* over its predictions. At the same time, it should confidently and consistently assign zero probability to certain states of the world if they are invalid, i.e., if they are violating *constraints*. These constraints can encode prior knowledge such as explicit rules [Marconato et al., 2023, 2024, Bortolotti et al., 2024] that can be crucial for the safety of the system and its users. For instance, they can encode that self-driving cars should avoid crashing into obstacles or go off-road [Xu et al., 2020, Giunchiglia et al., 2023].

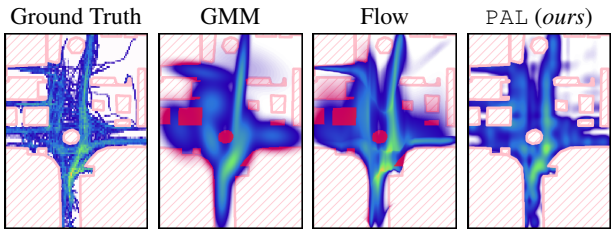

Figure 1: **PAL is guaranteed to place probability mass only within a given constraint** here represented as the (non deleted) walkable area of a map from the Stanford Drone Dataset, while unconstrained distribution estimators violate the constraint (area shown in red). See Section 7.3.

The promise of probabilistic neuro-symbolic (NeSy) methods [Garcez et al., 2019, 2022, De Raedt et al., 2021] for trustworthy AI is to integrate symbolic reasoning over these high-level constraints into neural predictors. The simplest way to achieve this is to encourage constraint satisfaction via a loss penalty at training time [Xu et al., 2018, Fischer et al., 2019, De Smet et al., 2023a]. However, such an approach might have catastrophic consequences at test time, as it does not *guarantee* that invalid configurations will be associated exactly probability zero: even a probability of 0.001% to violate a constraint can be considered harmful in safety-critical applications such as autonomous driving.

A number of recent works overcome this issue by proposing architectures that *certify the satisfaction of given constraints by design* [Manhaeve et al., 2018, Giunchiglia and Lukasiewicz, 2020, Ahmed et al., 2022a, Hoernle et al., 2022]. Unfortunately, they mostly consider constraints over Boolean or discrete variables only [De Smet and Dos Martires, 2024] and extending them to continuous variables is highly non trivial. This is because tackling constraints over *continuous* variables poses unique challenges. First, ensuring modeling a proper distribution over the constraint, i.e., renormalizing a density such that it exactly integrates to 1, is a #P-hard problem [Baldoni et al., 2008] even when the

distribution and constraints have a relatively simple structure [Zeng et al., 2020b,a]. Second, real-world constraints over continuous variables come in the form of intricate *algebraic* relationships [Barrett et al., 2021, Morettin et al., 2017]. Even considering simple linear inequalities among variables will entail that the support of the induced densities can take the form of (disjunctions of) non-convex polytopes [Stoian and Giunchiglia, 2025]. While focusing on single convex polytope constraints can be easier [Stoian et al., 2024c], it fails to capture real-world scenarios, such as modeling multiple obstacles that need to be avoided simultaneously on a map (Fig. 1). Scalability during learning is another major concern, as one would ideally want to compute fast and exact gradients for each data point. In practice, this is sometimes achieved by approximating or relaxing the constraint [De Smet et al., 2023a,b] thus giving up learning by exact maximum likelihood.

In this work, we narrow these gaps by introducing a *probabilistic algebraic layer* (PAL) that can be seamlessly plugged as the last layer into any neural architecture while guaranteeing probabilistic predictions to satisfy complex algebraic constraints. Our formulation for PAL uses a symbolic integration scheme that scales gracefully as it can be amortized, i.e., computed once for all datapoints, while allowing for exact gradients and hence exact maximum likelihood training, that is being retro-compatible with out-of-the-box optimizers using automatic differentiation.

Contributions. After formalizing the problem of probabilistic prediction over algebraic constraint in Section 2, we **C1)** introduce PAL and its ingredients while discussing its properties in Section 3; then we **C2)** introduce the GPU-accelerated symbolic polynomial integrator that powers PAL in Section 4. Finally, we **C3)** run an extensive set of experiments, comprising both standard benchmarks for algebraic constraint integration and real-world trajectory data from the Stanford drone dataset [Robicquet et al., 2016], which we augment by manually segmenting constraints representing obstacles and buildings.

2 PROBABILISTIC PREDICTIONS UNDER ALGEBRAIC CONSTRAINTS

Notation. Uppercase letters denote random variables (X, Y) and lowercase letters denote their assignments (x, y). We use bold for sets of variables $(\mathbf{X}, \mathbf{Y})$, and their joint assignments $(\boldsymbol{x}, \boldsymbol{y})$. We use lowercase Greek letters for denoting algebraic constraints (ϕ) and uppercase Greek letters for denoting (vectors of) learnable parameters. We say that $\boldsymbol{y}$ satisfies ϕ (written $\boldsymbol{y} \models \phi$) if and only if substituting $\mathbf{Y}$ with $\boldsymbol{y}$ in ϕ makes ϕ true. We denote the indicator function as $\mathbb{1}\{.\}$, therefore, $\mathbb{1}\{\mathbf{Y} \models \phi\}$ evaluates to 1 for all the values of $\mathbf{Y}$ satisfying ϕ and 0 otherwise.

Setting. We aim at learning a parameterized conditional distribution of $\mathbf{Y}$ given $\mathbf{X}$, i.e. $p_{\boldsymbol{\Theta}}(\mathbf{Y} \mid \mathbf{X})$, from a dataset $\mathcal{D} = (\boldsymbol{x}^{(i)}, \boldsymbol{y}^{(i)})$ of realizations of mixed continuous and discrete variables $\mathbf{X}$ and $\mathbf{Y}$. As discussed later, the challenge will be when some $\mathbf{Y}$ are continuous, and we can always assume all of them to be continuous without loss of generality. Differently from a classical supervised learning scenario, the support of $p_{\boldsymbol{\Theta}}$ is not the whole $\mathbb{R}^{|\mathbf{Y}|}$, but a restriction encoded by a constraint ϕ defined over $\mathbf{Y}$. This constraint encodes which regions of the label space are invalid, i.e., should have exactly zero-probability and therefore should not be sampled nor predicted [Grivas et al., 2024]. We give an example next.

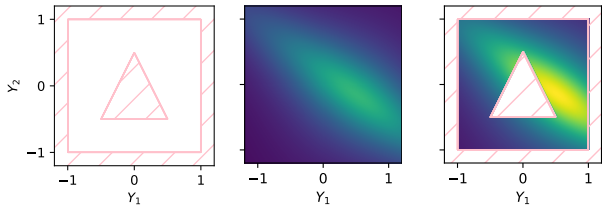

Figure 2: **A renormalized constrained density** (right) obtained by applying **non-convex algebraic constraints** (left) over an unconstrained distribution (middle).

Which constraints? We focus on algebraic constraints as Boolean combinations of linear inequalities, which are flexible enough to represent complex supports in the form of disjunctions of non-convex polytopes. We do so in the language of (quantifier-free) *satisfiability modulo linear real arithmetic* (SMT($\mathcal{LRA}$)) formulas [Barrett et al., 2021]. A constraint in SMT($\mathcal{LRA}$), from here on simply SMT formula or constraint, is a logical formula with arbitrary combinations of the usual Boolean connectives $(\wedge, \vee, \neg)$ over atoms that are restricted to linear inequalities over $\mathbf{Y}$:

$$\left(\sum\nolimits_i a_i Y_i \bowtie b\right) \quad a_i, b \in \mathbb{Q},\ \bowtie \in \{\leq, <, \geq, >, =\}.$$

Example. Consider the problem of learning a conditional distribution $p(Y_1, Y_2 \mid X_1, X_2)$ subject to the following constraint ϕ: $\mathbf{Y} \in [-1, 1]^2 \wedge \mathbf{Y} \notin \triangle$, where $\triangle$ denotes the triangle with vertices $(-0.5, -0.5)$, $(0, 0.5)$ and $(0.5, -0.5)$, as illustrated in Fig. 2 (left). We can encode such a constraint into SMT($\mathcal{LRA}$) as:

$$\phi = (-1 \leq Y_1) \wedge (Y_1 \leq 1) \wedge (-1 \leq Y_2) \wedge (Y_2 \leq 1) \wedge$$
$$[(Y_2 < -0.5) \vee (2Y_1 + 0.5 < Y_2) \vee (-2Y_1 + 0.5 < Y_2)]\,.$$

In the more realistic obstacle-avoidance example in the introduction (Fig. 1), ϕ can model the surface where cars and pedestrians are allowed to move. One principled solution to design a conditional distribution $p_{\boldsymbol{\Theta}}$ that is constraint-aware is to realize a *product of experts* [Hinton, 2002]

$$p_{\boldsymbol{\Theta}}(\mathbf{Y} \mid \mathbf{X} = \boldsymbol{x}) \propto q_{\boldsymbol{\Theta}}(\mathbf{Y} \mid \boldsymbol{x}) \mathbb{1}\{\mathbf{Y} \models \phi\} \tag{1}$$

where $q_{\boldsymbol{\Theta}}$ is an unconstrained density whose support is the full $\mathbb{R}^{|\mathbf{Y}|}$ (Fig. 2, middle) and $\mathbb{1}\{\mathbf{Y} \models \phi\}$ encodes the sat-

isfaction of the constraint ϕ. Unfortunately Eq. (1) alone does not encode a proper density, as it does not integrate to 1. Alternative ways to train such a product of experts are possible [Hinton, 2002], but they are not retro-compatible with the usual gradient-based optimization recipe to train neural networks: maximum likelihood estimation (MLE). To learn the parameters $\boldsymbol{\Theta}$ by *exact* MLE, and hence to design a layer can be seamlessly plugged-in any network, we would need to compute its renormalization constant, i.e.,

$$\int q_{\boldsymbol{\Theta}}(\boldsymbol{y} \mid \boldsymbol{x}) \mathbb{1}\{\boldsymbol{y} \models \phi\} \, d\mathbf{Y} \tag{WMI}$$

which is also known as a *weighted model integration* (WMI) problem [Belle et al., 2015], i.e., the probability that the constraint is satisfied, $\mathsf{Pr}(\phi)$. Appendix A discusses the background and literature behind WMI in depth.

Here we first note that we treat all variables $\mathbf{Y}$ in Eq. (WMI) to be continuous, something that we can do without loss of generality as we can always reduce a WMI problem over mixed discrete-continuous variables to one over continuous variables only without increasing the problem dimensionality [Zeng and Van den Broeck, 2019]. However, the complexity of solving a WMI problem exactly is #P-hard in general [Zeng et al., 2020a] and tractable algorithms are available only when the constraints ϕ come with certain structures [Zeng et al., 2020b]. In the need to scale the computation of Eq. (WMI), many NeSy approaches opted to *approximate* it. For example, DeepSeaProblog (DSP) [De Smet et al., 2023a] (see Section 6 for a discussion) designs a general probabilistic logic programming framework for WMI problems parameterized by neural networks. However, to practically compute the WMI integral, DSP employs rejection sampling. Not only does this require to relax the constraints to perform back-propagation, yielding high-variance gradients, but it also hinders scalability, as the WMI integral *needs to be approximated for each datapoint* $\boldsymbol{x}$.

To be able to scale neural networks with complex real-life constraints such as the ones in Fig. 1, while retaining constraint satisfaction guarantees, we have to push the current boundaries of the WMI literature. Next, we discuss how to do so while selecting a parametric form for $q_{\boldsymbol{\Theta}}$ (Section 3) that allows us to efficiently amortize the computation of the WMI integral into a symbolic computational graph that, once built, can leverage GPU parallelism (Section 4).

3 A PAL FOR GUARANTEED CONSTRAINT SATISFACTION

We devise a differentiable *probabilistic algebraic layer* (PAL) realizing the following conditional distribution:

$$p_{\boldsymbol{\Theta}}(\mathbf{Y} \mid \boldsymbol{x}) = \frac{q(\mathbf{Y}; \boldsymbol{\lambda} = f_{\boldsymbol{\psi}}(\boldsymbol{x})) \mathbb{1}\{\mathbf{Y} \models \phi\}}{\int q(\boldsymbol{y}'; \boldsymbol{\lambda} = f_{\boldsymbol{\psi}}(\boldsymbol{x})) \mathbb{1}\{\boldsymbol{y}' \models \phi\} \, d\mathbf{Y}'} \tag{PAL}$$

where $\boldsymbol{\Theta} = \{\boldsymbol{\lambda}, \boldsymbol{\psi}\}$ and $q(\mathbf{Y}; \boldsymbol{\lambda} = f_{\boldsymbol{\psi}}(\boldsymbol{x}))$ is a flexible unconstrained distribution whose parameters $\boldsymbol{\lambda}$ are the output of a neural backbone $f_{\boldsymbol{\psi}}$ that takes as input $\boldsymbol{x}$ and ϕ encodes an SMT constraint as discussed above. As discussed in Section 2, this construction guarantees that the density $p_{\boldsymbol{\Theta}}$ is non-zero only inside the region defined by ϕ (Fig. 2, right). Note that our layer can be used as a standalone distribution estimator when there are no input variables to condition on, i.e., to model $p_{\boldsymbol{\lambda}}(\mathbf{Y})$.

We can design a neural backbone $f_{\boldsymbol{\psi}}$ by easily reusing any existing architecture. Given any (possibly pretrained) neural network $\boldsymbol{z} = h(\boldsymbol{x})$ that outputs an embedding $\boldsymbol{z}$ for each datapoint $\boldsymbol{x}$, in fact we can realize f as $\boldsymbol{\lambda} = g(h(\boldsymbol{x}))$ by adding a simple *gating function* g that maps $\boldsymbol{z}$ to $\boldsymbol{\lambda}$. Less trivial is to select a suitable model family for $q_{\boldsymbol{\lambda}}$ that allows us to efficiently amortize the computation of the denominator of PAL. If we had to deal *only* with Boolean variables $\mathbf{Y}$ and propositional constraints ϕ, we could leverage probabilistic circuits (PCs) [Darwiche and Marquis, 2002, Choi et al., 2020], compact multilinear polynomials over tractable functions as in Ahmed et al. [2022a]. Unfortunately, there is no equivalent circuit representation for SMT constraints with the required structural properties to guarantee tractability [Vergari et al., 2021].

General polynomials to the rescue. Whereas we cannot leverage the properties of structured polynomials such as PCs, we can still employ general (piecewise) polynomials to model the unconstrained density $q_{\boldsymbol{\lambda}}$ in PAL. They will still provide *expressiveness* as they can approximate any density up to arbitrary precision [Morettin et al., 2021, Cheng et al., 2024] and, more crucially, they are closed under integration over a polytope [Zeng et al., 2020b]. The general form of polynomials we consider is therefore:

$$q(\boldsymbol{y}; \boldsymbol{\lambda}) = \sum_{i=1}^{M} \lambda_i \prod_j y_j^{\alpha_{ij}} \tag{2}$$

where each coefficient $\lambda_i \in \mathbb{R}$ is one of the outputs of the backbone $f_{\boldsymbol{\psi}}$ and the exponents $\alpha_{ij} \in \mathbb{N}$ are constant parameters. As we will discuss in the next section, the complexity of integration will depend, among other things, on the degree of the polynomial and on the number of monomials M. At the same time, this will offer the opportunity to design a fixed-parameter tractable integration scheme, as we can bound the polynomial degree by construction.

How to construct polynomials? We can generate polynomial structures in an exhaustive way given a max degree d, i.e., by generating all possible monomials with degree $\leq d$, or by randomly subsampling them in order to have a compact polynomial of high degree. Alternatively, we can use piecewise polynomials such as *splines*, which have been demonstrated to be very expressive in ML, even with low degree [Durkan et al., 2019]. In particular, in our experiments, we use cubic Hermite splines [Smith, 1980], see Appendix B.2 for details.

Whereas all the aforementioned polynomials can always be rewritten in the canonical form of Eq. (2), they might not guarantee to model a valid density as they might yield negative values. To this end, we propose to use *squared polynomials* in PAL, which have been recently investigated in the PC literature for their expressiveness properties [Loconte et al., 2024, 2025b, Loconte and Vergari, 2025]. Specifically, we consider sum of squared polynomials, i.e., polynomials of the form:

$$\sum_k w_k \left(\sum_i u_i \prod_j y_j^{\alpha_{ijk}} \right)^2 \tag{3}$$

where $w_k > 0$ and $u_i \in \mathbb{R}$ and therefore where $\boldsymbol{\lambda} = \{w_k\}_k \cup \{u_i\}_i$ when we rewrite Eq. (3) into Eq. (2). Now we have all the ingredients to discuss how to parallelize the computation of the denominator in PAL.

4 EXTREME PARALLELIZATION OF POLYNOMIAL INTEGRALS ON A GPU

State-of-the-art (SoTA) WMI solvers propose various ways to break the WMI integral over ϕ into smaller integrals over disjoint convex polytopes $\mu_1, ...\mu_K$ such that $\bigvee_i \mu_i \equiv \phi$. Hence, from here on, we will focus on the problem of integrating a polynomial in canonical form (Eq. (2)) over a single convex polytope. *Our solution to scale the computation of this simpler problem will therefore speed up any SoTA WMI solver*. In practice, for PAL we will adopt SAE4WMI [Spallitta et al., 2024] to break ϕ into $\mu_1, ...\mu_K$, as it is the most advanced WMI solver that deals with arbitrary non-convex algebraic constraints ϕ at the time of writing. See Appendix A for a discussion.

Our solution, named GPU-Accelerated Simplicial !ntegrator (`GASP!`), builds upon the idea that we can *compile once* the WMI integral into a highly-parallelizable computational graph $I_\phi(\boldsymbol{\lambda})$ that is a function over the polynomial parameters $\boldsymbol{\lambda}$, and reuse this compiled function to amortize the evaluation of the denominator of PAL for every datapoint $\boldsymbol{x}$. In fact, we can rewrite the WMI integral over a convex polytope μ as a sum of integrals over monomials:

$$\begin{aligned} I_\phi(\boldsymbol{\lambda}) &= \int q(\boldsymbol{y}; \boldsymbol{\lambda}) \mathbb{1}\{\boldsymbol{y} \models \mu\} \, d\mathbf{Y} \\ &= \sum_i \lambda_i \int \prod_j y_j^{\alpha_{i,j}} \mathbb{1}\{\boldsymbol{y} \models \mu\} \, d\mathbf{Y} = \sum_i \lambda_i \eta_i. \end{aligned}$$

By treating $\boldsymbol{\lambda}$ as symbolic variables, we have no dependence on $\mathbf{X}$ anymore, and we recover $I_\phi(\boldsymbol{\lambda})$ as a symbolic polynomial whose coefficients are the results of the monomial integrals $\eta_i = \int \prod_j y_j^{\alpha_{i,j}} \mathbb{1}\{\boldsymbol{y} \models \mu\} \, d\mathbf{Y}$. Note that solving all these integrals is an embarrassingly parallelizable problem (see Appendix C.1). While in principle one could use a symbolic solver such as sympy [Meurer et al., 2017a], or another exact WMI solver, these are extremely slow in practice and won't allow `PAL` to scale, as we empirically confirmed in Section 7.1.

Algorithm 1 GASP!$(q, \mathbf{H})$

Input polynomial q and a convex polytope $\mathbf{H}$
Output The Integral $\int_{\mathbf{H}} \hat{q}(\boldsymbol{y}) d\mathbf{Y}$

1: $d \leftarrow \mathsf{totalDegree}(q)$
2: $(\mathbf{R}, \mathbf{w}) \leftarrow \mathsf{prepareGrundmannMöller}(d, \dim(\mathbf{H}))$
3: {points and weights of the cubature, see algorithm 4}
4: $\mathbf{V} \leftarrow \mathsf{HtoVDescription}(\mathbf{H})$
5: {turns inequalities into vertices spanning $\mathbf{H}$}
6: $\mathbf{S} \leftarrow \mathsf{Triangulate}(\mathbf{V})$ {obtain simplices}
7: **return** $\mathsf{GASPCubature}(\hat{q}, (\mathbf{R}, \mathbf{w}), \mathbf{S})$

Algorithm 2 GASPCubature$(q, (\mathbf{R}, \mathbf{w}), \mathbf{S})$

Input a polynomial q, cubature points $\mathbf{R} \in \mathbb{R}^{l_{gm} \times n}$ and weights $\mathbf{w} \in \mathbb{R}^{l_{gm}}$, simplices $\mathbf{S} \in \mathbb{R}^{l_s \times (n+1)}$
Output the integral $\sum_i \int_{s_i} \hat{q}(\boldsymbol{y}) d\mathbf{Y}$

1: $r_{gasp} \leftarrow \mathsf{Array}(\mathsf{Length}(\mathbf{S}))$
2: **for** $i \leftarrow 1$ **to** $\mathsf{Length}(\mathbf{S})$ **do** {this loop runs in parallel}
3: $\quad \mathbf{r}_{gm} \leftarrow \mathsf{array}(\mathsf{length}(x))$
4: $\quad vol \leftarrow \mathsf{volume}(\mathbf{S}[i])$
5: $\quad$ **for** $j \leftarrow 1$ **to** $\mathsf{length}(\mathbf{R})$ **do**
6: $\quad\quad$ {this loop runs batched (e.g., 512 points)}
7: $\quad\quad \boldsymbol{x} \leftarrow \mathsf{coordinateChange}(\mathbf{R}[j], \mathbf{S}[i])$
8: $\quad\quad$ {transform from unit simplex to s_i}
9: $\quad\quad \mathbf{r}_{gm}[j] \leftarrow w[j] \cdot \mathsf{polyEval}(\hat{q}, \boldsymbol{x})$
10: $\quad\quad$ {monomials are evaluated in parallel in polyEval}
11: $\quad$ **end for**
12: $\quad \mathbf{r}_{gasp}[i] \leftarrow vol \cdot \mathsf{stableSum}(\mathbf{r}_{gm})$
13: **end for**
14: **return** $\mathsf{stableSum}(\mathbf{r}_{gasp})$

To fully harness GPUs acceleration, we look at ways of further parallelizing the integration of each monomial. An approximate solver such as Sampo [Dos Martires et al., 2019] could leverage the GPU to perform rejection sampling. However, the quality of this approximation scheme will degrade quickly with the number of dimensions and complexity of ϕ, as observed in Section 7.1.

Our `GASP!` pushes parallelism to the limit and consists of a further decomposition in sub-problems (Algorithm 1) which in turn are run as small numerical quadrature tasks that can fully leverage the tensor operations of a GPU (Algorithm 2). In a nutshell, we aim to integrate monomials via the Grundmann and Möllers integration formula [Grundmann and Möller, 1978], which is a simple cubature rule that however operates on the unit-simplex.

Therefore, we first decompose each convex polytope μ into simplices using Delaunay triangulation[1] (L5−7 in Algorithm 1). Then we transform all these simplices in unit-

[1]We use the QHull library [Barber et al., 1996].

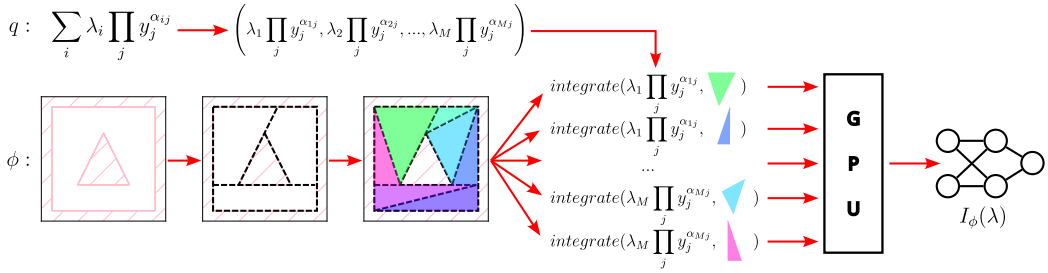

Figure 3: **An overview of our pipeline with GASP!**. The integrand q is decomposed into parallelizable monomial integrations (*top*). The non-convex constraint is first decomposed into several convex regions (Appendix A) that are further decomposed into (colored) simplices (*bottom*). The resulting computational graph is highly parallelizable on a GPU.

simplices (L5,8 and 12 in Algorithm 2). We finally apply the Grundmann and Möllers cubature rule which reduces to the evaluation of the (transformed) monomials at specific points on the unit-simplex, summing them according to some precomputed weights. This cubature rule guarantees exact integration by generating a number of points that is a function of the polynomial degree. Fig. 3 provides an overview of the full integration pipeline in GASP!. Note that GASP! can be used also as a *standalone* numerical integrator for polynomials, e.g., when there is no neural network f_{ψ} and the coefficients $\boldsymbol{\lambda}$ are constants.

Complexity. Integrating an arbitrary polynomial on a convex polytope is an NP-hard task, which however becomes tractable if the dimensionality is bounded while the polynomial degree and the dimension of the simplex are allowed to vary [Baldoni et al., 2011]. Our scalability will therefore depend on the complexity of the constraint ϕ through the number of simplices, on the polynomial degree through the number of monomials and cubature points, and finally on the number of dimensions we integrate over. Appendix C.2 provides an in-depth discussion of how these parameters impact GASP!. Additionally, we expand on the overall complexity of PAL in relationship to the constraint ϕ and w.r.t. the number of bins for the piecewise spline. We remark that we have to run GASP! *only once*, before training, and we can reuse the computational graph $I_{\phi}(\boldsymbol{\lambda})$ for all datapoints $\boldsymbol{x}$, greatly amortizing computation (see Fig. 4).

5 PROBABILISTIC REASONING WITH PAL

As GASP! allows us to feasibly marginalize out all variables $\mathbf{Y}$ in order to compute the WMI integral, it allows us also to compute arbitrary marginals as we integrate out a subset of $\mathbf{Y}$. This enables PAL to query for the probability of different events defined over the labels. Specifically, it crucially allows us to answer other probabilistic reasoning tasks at *test time*, such as exactly computing the probability of satisfying (or violating) a *new* constraint, e.g., the area around a new obstacle that just appeared on a map like Fig. 1. This can be easily done by computing $\mathsf{Pr}(\phi \wedge \gamma)/\mathsf{Pr}(\phi)$ where $\mathsf{Pr}(\phi)$ is the usual WMI integral, $\phi \wedge \gamma$ the conjunction of the old SMT constraint ϕ with a new one γ (e.g., representing the obstacle) over which one can compute the updated WMI probability $\mathsf{Pr}(\phi \wedge \gamma)$.

Sampling with GASP! As GASP! allows us to marginalize out all variables $\mathbf{Y}$ in order to compute the WMI integral, it allows us also to compute arbitrary marginals as we integrate out a subset of $\mathbf{Y}$. This in turn enables us to draw samples from PAL that naturally satisfy the constraint ϕ without rejection but using inverse transform sampling. Given a variable ordering $Y_1, Y_2, \ldots, Y_n$, we can *iteratively* sample $y_1 \sim p(Y_1|\boldsymbol{x})$ and $y_i \sim p(Y_i|y_{<i}, \boldsymbol{x})$ for $i \in \{2, ..., n\}$, where each sampling step requires numerically inverting the corresponding conditional cumulative distribution function (another WMI integral computable with GASP!), which can be efficiently done via binary search. This procedure is detailed in Appendix F.

6 RELATED WORK

Many probabilistic NeSy [Marra et al., 2024] approaches try to satisfy constraints only *in expectation*. These include incorporating the constraints as a loss term, applied to various formalisms such as propositional logic [Xu et al., 2018, Ahmed et al., 2023], fuzzy logic [Diligenti et al., 2017], physical laws [Stewart and Ermon, 2017] or other algebraic constraints on the outputs of the NNs [Fischer et al., 2019]. Compared to PAL, these approaches do not guarantee the satisfaction of the constraints.

A series of other works, instead, guarantees the satisfaction of constraints by *embedding* them in the network architecture. For example, Stoian et al. [2024a,b] take a similar approach to PAL, by adding a constraint layer on top of NNs, which however is limited to constraints in the form of conjunctions of inequalities. Stoian and Giunchiglia [2025] goes beyond this limitation and devise a layer that projects samples into non-convex constraints. Differently from us, these layers do not yield densities or probabilities associated to the sampled points or to given constraints. How-

ever, their sampling schemes scale much better than autoregressive sampling with PAL. Multiplexnet [Hoernle et al., 2022] introduces a layer restricted to constraints in disjunctive normal form, which must be relaxed during learning. As a result, it struggles to scale to the intricate constraints in our setting. DeepSade [Goyal et al., 2024] takes a different route, pairing gradient descent with constrained optimization to guarantee SMT constraints for classification and regression tasks. This approach supports SMT formulas with quantifiers, however, its extension to the probabilistic setting is highly non-trivial. Our work is inspired by semantic probabilistic layers (SPL) [Ahmed et al., 2022b], which combines neural networks with probabilistic circuits [Loconte et al., 2025a] in the propositional logic case. We generalize SPL to constraints involving both logical and continuous variables. Similar to SPL, DeepProbLog [Manhaeve et al., 2021] uses probabilistic logic programming to create a layer, but considers only Boolean logic and fully-factorized distributions [van Krieken et al., 2024].

As discussed in Section 2, closer to our work is DeepSeaProbLog (DSP) [De Smet et al., 2023a], which extends DeepProbLog to continuous domains. In contrast to PAL, in their implementation, densities are not guaranteeing constraint satisfaction. In fact, DSP is trained to maximize the probability of the constraint being satisfied, i.e., the WMI integral, via sampling. We detail the DSP-Loss in the appendix. As a side effect, one cannot avoid the rejection layer in DSP as samples directly drawn from the unconstrained probability of a DSP program can violate the constraints. Appendix D discusses additional related works.

7 PAL IN ACTION

In this section, we aim to answer the following research questions:[2] **RQ1** How does GASP! compare with other integration solvers? **RQ2** Can PAL learn and scale with an increasing number of constraints? **RQ3** Can PAL handle real-world data and its constraints?

7.1 RQ1) BENCHMARKING GASP!

We compare GASP! first against approximate numerical schemes such as rejection sampling, which is commonly used to scale probabilistic NeSy approaches such as DSP (Section 6), and then against SoTA exact polynomial integrators such as LattE [Baldoni et al., 2014].

GASP! vs numerical approximations for PAL. We evaluate GASP! w.r.t. an implementation of rejection sampling that runs on the GPU, on random non-convex integration problems of increasing dimensionality and degree. Appendix E.1 details this experimental setting and Fig. 12

[2]The source code and the instructions to reproduce our results can be found at: github.com/april-tools/pal

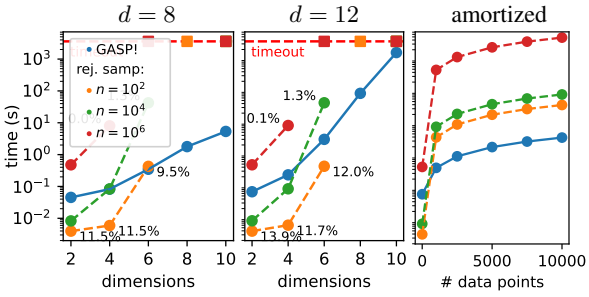

Figure 4: *Left* and *center*: runtime of GASP! and rejection sampling (using $10^{\{2,4,6\}}$ samples) on integrals over 4 random simplices for increasing dimensions. We report the relative error (%) for rejection sampling. *Right*: Our amortization speed-up compared to rejection-sampling in 2-dimensions for the 12-degree polynomial. Fig. 12 shows more results for different degrees and constraints.

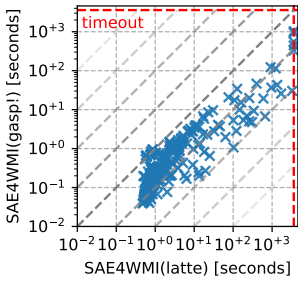

Figure 5: **GASP! can be 1 to 2 orders of magnitude faster than a SoTA polynomial integrator** such as LattE when evaluated on standard WMI benchmarks from Spallitta et al. [2024]

reports all results. Here we show in Fig. 4 (*left* and *center*) how rejection sampling struggles to obtain accurate results in higher dimensions for a fixed time budget (1 hr) and polynomials of degree 8 and 12, as the number of rejected samples grow exponentially. Notably, the complexity of the constraints is fixed in this experiment to 4 random simplices. We expect rejection sampling to perform much worse with increasingly complex regions. GASP! instead provides exact computation and scales better (notice that the y-axis is log-scale). More crucially, GASP! can amortize computation as the compiled polynomial $I_\phi(\boldsymbol{\lambda})$ can be reused throughout the training of PAL. Fig. 4 (*right*) illustrates this for a degree 12 polynomial in 10 dimensions: integrating over a single convex polytope for 10^4 predictions, i.e. 10^4 different values for $\boldsymbol{\lambda}$, takes less then 10 seconds with GASP! thanks to the amortization and up to 1 hour with rejection sampling. This is fundamental to use GASP! in PAL, as the number of evaluations of WMI integrals can easily be orders of magnitude larger than that.

GASP! as a stand-alone integrator. We compare GASP! against LattE, a SoTA exact polynomial integrator based on cone decomposition [Baldoni et al., 2014], in the context of WMI integration (details in Appendix E.2). We adopt SAE4WMI (also used in PAL, see Section 4), and compare it while using either GASP! or LattE on 270 WMI in-

Figure 6: While PAL naturally handles constraints on the N-Star, the neural network + GMM has trouble fitting both constraints and data. More quantitative results in Table 1 and qualitative ones in Appendix E.3.1.

stances of varying complexity taken from Spallitta et al. [2024]. Compared to the previous experiment, these WMI problems are highly non-convex, requiring the computation of up to hundreds of integrals each. Notably, here GASP! cannot harness its amortization capabilities and needs to instantiate a different computational graph every time. Despite this, GASP! proves faster than LattE in 263 instances over 270, speeding computation up to one or two orders of magnitude, as shown in Fig. 5. Lastly, and as a sanity check, we compare GASP! against classical symbolic integrators such as sympy in Appendix E.2.1. While we retrieve the same computation, we achieve a speed up of 1200 times. Overall, our results confirm that GASP! is the best available solver for PAL, positively answering **RQ1**.

7.2 RQ2) SCALING CONSTRAINTS WITH PAL

In this experiment, we evaluate PAL in a controlled setting to explore how accurately learning in PAL scales when increasing the number of constraints, while keeping the dimensionality fixed. The task is learning the distribution $p(Y_1, Y_2 \mid X_1, X_2)$ constrained by a N-pointed star, as shown in Fig. 6, for $N = 7$ whose unconstrained distribution is a Cauchy with constant scale and mode $\mathbf{X}$. Table 1 reports the average test log-likelihood of PAL versus an unconstrained NN, a mixture density network [Bishop, 1994] with a Gaussian mixture model (GMM) with different components (K) as output, and DSP. All models use the same fully-connected NNs with ReLUs as a backbone. Appendix E.3.1 further details our setting.

As N increases, the gap between PAL and our the competitors widens as the mode tends to be closer to the extremes of the feasible region. Being agnostic to the constraint ϕ, the NN+GMM has an hard time fitting both the data and respecting the constraints. The same goes for DSP which is hindered by having to fit a single multivariate Gaussian while maximizing the mass inside ϕ, i.e., $\mathsf{Pr}(\phi)$, see DSP-Loss. This has often the unwanted effect of pushing the learned mode far from the target mode. This aspect prompted us to report the performance of DSP selecting the model according to best log-likelihood on holdout data as opposed to the standard best loss criterion. PAL in comparison has an easier time, it naturally handles constraints and therefore just has to move the probability mass around, prompting us to answer **RQ2** positively.

Table 1: **PAL can be more accurate than unconstrained networks and other NeSy baselines** in terms of average test log-likelihood on the NStar-dataset. We report the mean over 10 repetitions, more results in Appendix E.3.1.

	NN + PAL		NN + GMM		DSP	
N	$d=10$	$d=14$	K=8	K=32	by logLike	by Loss
3	-4.749	**-4.674**	-4.740	-4.723	-5.027	-42.821
7	-4.529	**-4.527**	-4.708	-4.612	-5.019	-206.411
11	**-4.570**	-4.584	-4.791	-4.620	-83.042	-43.151
19	-4.506	**-4.492**	-4.925	-4.652	-5.001	-155.139

7.3 RQ3) STANFORD DRONE DATASET

After showing PAL scalability to many constraints, we now evaluate it on real-world data where the ground truth is unavailable. As the majority of existing approaches are unable to process non-convex constraints (Section 6), established benchmarks are lacking. We fill this gap by introducing a new, challenging task based on the Stanford drone dataset (SDD) [Robicquet et al., 2016], which shoes aerial views of pedestrians, cars and bikes traversing different scenes in the Stanford campus. [3] We extract trajectories as in Wu et al. [2023] and we manually annotate two scenes, number 12, which contain the most trajectories, and 2, which contains highly non-convex constraints.

Specifically, we create constraints in SMT by segmenting the images over the areas that are non-walkable. Fig. 7 shows an example of an intersection from scene 12 and the extracted constraints. We evaluate two settings: where we model all trajectories together, and when the task is to probabilistically predict the future position given an observed partial trajectory. In contrast to RQ1 and RQ2, the probability mass in the SDD is less spread out and more localized at regions of high density. This setting is less suited to be modeled by a single polynomial and more applicable to a piecewise construction. We therefore choose Hermite splines because they are easy to train and scale well with our dataset. The exact construction of the splines is described in Appendix B.2.

Modeling joint trajectories ($p(\mathbf{Y})$). We tackle the problem of estimating the joint distribution of all trajectories, i.e., $p(\mathbf{Y})$. This means we optimize PAL as a standalone distribution estimator, without any neural backbone. Appendix E.4 details our experimental setting, in which we compare PAL with polynomial splines of increasing com-

[3] The dataset can be found at https://github.com/april-tools/constrained-sdd

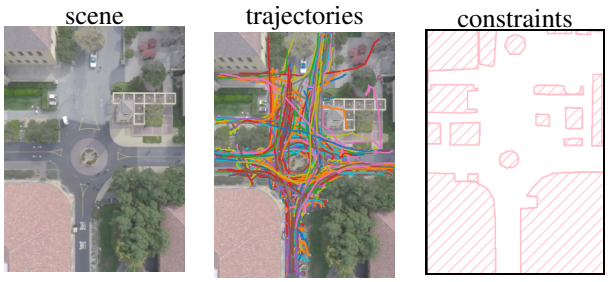

Figure 7: **Our dataset combines challenging constraints with real-world data** on trajectories (*middle*) and aerial maps (*left*) taken from Robicquet et al. [2016]. We manually label the data, segmenting invalid areas out (*right*).

Table 2: **PAL does not trade expressiveness for constraint-satisfaction** when compared against a GMM and a neural spline flow with t=1 and t=5 transformations, as it provides competitive average test log-likelihood but never violates constraints for test-set predictions ($\Pr(\neg\phi)$). We report the mean over 10 repetitions, more results in Appendix E.4. The setting is the unconditional $P(\mathbf{Y})$-case.

		PAL		GMM		Flow	
scene (params)		10 knots (410)	16 knots (650)	K=50 (300)	K=100 (610)	t=1 (2670)	t=5 (13350)
1	ll	−2.98	−2.93	−2.98	**−2.91**	−3.10	−2.94
	$\Pr(\neg\phi)$	**0.0%**	**0.0%**	≈2.3%	≈1.2%	≈5.6%	≈1.6%
2	ll	−3.35	−3.30	−3.34	**−3.26**	−3.43	−3.26
	$\Pr(\neg\phi)$	**0.0%**	**0.0%**	≈1.2%	≈0.6%	≈2.2%	≈0.7%

plexity against a GMM with increasing number of components and finally a neural spline flow [Durkan et al., 2019] with multiple transformation layers. PAL is able to achieve competitive test log-likelihoods w.r.t. similarly sized GMMs and much larger flows (with one order of magnitude more parameters), as reported in Table 2. More crucially, PAL never places probability mass outside the given constraint, while the other competitors do so as shown in Fig. 1 and under $p(\neg\phi)$ in Table 2, denoting the probability of bumping into an obstacle, here approximated with 10^6 samples for the GMM and the flow. Note that violating the constraint less than 2% of the time can still be greatly harmful for safety-critical applications. In summary, PAL is able to guarantee constraint satisfaction while not compromising accuracy, nor time. In fact, GASP ! takes only 17 seconds on an NVIDIA RTX A6000 to integrate the largest polynomial we consider (d=12) on the intricate constraint in Fig. 7 (right).

Modeling future positions ($p(\mathbf{Y} \mid \mathbf{X})$). After showing that our layer can effectively model the joint distribution, we consider estimating the distribution over future positions given some observations on the current trajectory. To this end, we subsample five equidistant points from a trajectory that we consider as input variable $\mathbf{X}$, and we predict the

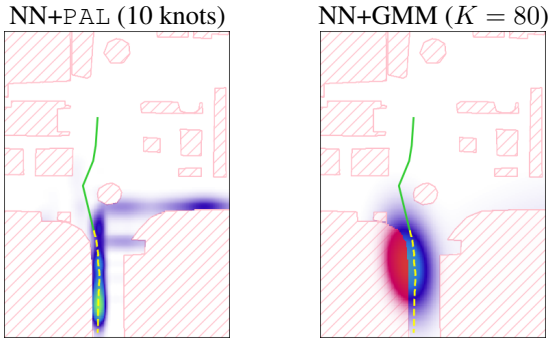

Figure 8: **PAL captures meaningful modes when modelling how a trajectory might evolve ($p(\mathbf{Y} \mid \mathbf{X})$) while never violating the constraint** differently from a NN with a GMM output. The observed test trajectory and ground-truth on scenario 1 completion are reported in green/solid and dashed/yellow. Additional plots in Table 20.

probability of the model of being in any other point Y_1, Y_2 in the map. Appendix E.5 completely details our stoetting.

Figure 8 and 9 depict the conditional distributions modeled by PAL and NN+GMM for a single observed trajectory. As expected, multiple future trajectories are visible in the distribution modelled by PAL. In contrast, the conditional GMM is less good at capturing the multimodality of $p(\mathbf{Y} \mid \mathbf{X})$, while also clearly violating the constraints. Table 3 reports a quantitative comparison of NN+PAL with NN+GMM and DSP (finer grained results are reported in Table 19 and 22) showing the average log-likelihood of the points in the (unobserved) trajectory completions and the average probability of sampling future positions that violate ϕ (estimated using 10^6 samples for NN+GMM and DSP). We do not compare against flows in this setting, as parameterized them with a neural network turned out infeasible: it would have required millions of parameters just to realize a linear gating function g (Section 3). Results in Table 3 show that the constraint violation is on average around the 18% for the baselines across all trajectories. This value raises up to 70% for the GMM model on certain trajectories. We highlight that the probability of violating the constraint is higher for conditional predictions because of less data: having direct access to the constraint ϕ greatly improve data efficiency for PAL.

All in all, these results show that PAL, both alone and combined with NNs and in contrast to the other baselines, show promise in effectively modelling complex real world distributions, without trading off expressiveness for constraint satisfaction. We answer **RQ3** positively.

8 CONCLUSION

In this work, we introduced PAL, a probabilistic NeSy layer that can be plugged as the prediction layer in any neural net-

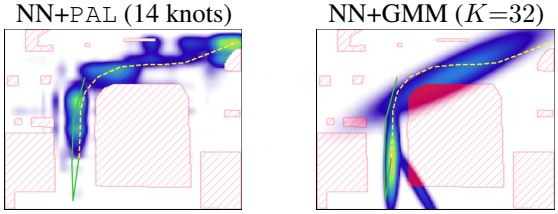

Figure 9: **PAL wraps around the boundaries of our constraints**, in contrast to the NN with an GMM, which predicts a trajectory straight trough the constraint. The observed test trajectory and ground-truth completion on scenario 2 are reported in green/solid and dashed/yellow respectively.

Table 3: **PAL shows competitive likelihoods while guaranteeing constraint-satisfaction** when compared to neural GMM and DSP, for which we provide statistics for the fitted neural distributional fact. We approximate the probability of violating the constraints ($\mathsf{Pr}(\neg\phi)$) at test time numerically per data point and average it. We report the mean over 10 repetitions, further details in Table 19 and Table 22. The setting is the conditional $P(\mathbf{Y}|\mathbf{X})$-case.

		NN + PAL		NN + GMM		DSP
scene		10 knots	14 knots	K=50	K=100	-
1	ll	**−2.08**	−2.27	−2.64	−2.83	−3.87
	$\mathsf{Pr}(\neg\phi)$	**0%**	**0%**	≈21%	≈20%	≈ 49%
2	ll	−2.23	**−2.09**	−2.39	−2.42	−3.61
	$\mathsf{Pr}(\neg\phi)$	**0%**	**0%**	≈15%	≈14%	≈ 36%

work that has to deal with multiple continuous labels and in the presence of algebraic constraints over them. To scale PAL to real-world data, we had to advance the field of WMI by proposing GASP!, a parallelizable polynomial integrator that challenges even established scientific software such as LattE reaching a speed-up of up to one or two orders of magnitude. Furthermore, PAL offers flexible marginalization over new constraints at test time. While this also allows us to use GASP! to sample from PAL, it does not allow us to easily tackle maximum a posteriori (MAP) in a similar way. How to compute MAP-style queries for PAL remains an open research question [Zeng et al., 2021]. In the future, we plan to investigate and scale GASP! further as a standalone software for a number of computationally intense applications using polynomials such as inference in Bayesian [Zeng and Van den Broeck, 2023] and physics informed neural networks [Lu et al., 2021].

At the same time, PAL offers a number of interesting future directions such as enforcing constraints in several applications ranging from fairness [Pfrommer et al., 2022, Ren et al., 2024] to climate modeling [Beucler et al., 2021, Harder et al., 2023, Willard et al., 2020, Beucler et al., 2020] and probabilistic verification [Morettin et al., 2024]. Furthermore, we plan to extend PAL to deal with more types of constraints than SMT($\mathcal{LRA}$). Building on the work of Chin and Sukumar [2020], we aim to extend GASP! to handle parametric curved boundaries, such as B-splines. This would then unlock further applications, e.g. in engineering, as it allows us to apply PAL to domains defined by NURBS surfaces, a common format to describe shapes in engineering design.

Author Contributions

AV, RS and AP discussed to extend SPL to algebraic constraints and LK and AV conceptualized a way to do so, which resulted in PAL. LK is responsible for coming up with GASP! and for the design and implementation of all experiments and plots with the exception of experiment 7.1, which was contributed by PM. AV, PM and LK wrote the paper. AV supervised and provided feedback for all the phases of the project with help from RS and AP.

Acknowledgements

We are grateful to Lennert De Smet and Pedro Zuidberg Dos Martires for insightful discussions regarding both the experimental evaluation and the general direction of the project, particularly in comparing DeepSeaProbLog and PAL. Additionally, we thank Adrián Javaloy, Gennaro Gala, Andreas Grivas for valuable feedback on the draft. AV was supported by the UNREAL: Unified Reasoning Layer for Trustworthy ML project (EP/Y023838/1) selected by the ERC and funded by UKRI EPSRC. PM was supported by the MSCA project Probabilistic Formal Verification for Provably Trustworthy AI - PFV-4-PTAI under GA no. 101110960. RS was supported in part by the MUR PNRR project FAIR - Future AI Research (PE00000013) funded by the NextGenerationEU. AP and RS were supported by the TANGO project funded by the EU Horizon Europe research and innovation program under GA No 101120763. Funded by the European Union. RS was supported in part under the NRRP, Mission 4 Component 2 Investment 1.4, by the European Union - nextGenerationEU (proj. nr. CN 00000013). Views and opinions expressed are however those of the author(s) only and do not necessarily reflect those of the European Union, the European Health and Digital Executive Agency (HaDEA) or The European Research Council. Neither the European Union nor the granting authority can be held responsible for them.

References

Ralph Abboud, İsmail İlkan Ceylan, and Radoslav Dimitrov. Approximate weighted model integration on dnf structures. *Artificial Intelligence*, 311:103753, 2022.

Hadi Mohasel Afshar, Scott Sanner, and Christfried Webers. Closed-form gibbs sampling for graphical models with algebraic constraints. In Dale Schuurmans and Michael P. Wellman, editors, *Proceedings of the Thirtieth AAAI Conference on Artificial Intelligence, February 12-17, 2016, Phoenix, Arizona, USA*, pages 3287–3293. AAAI Press, 2016. doi: 10.1609/AAAI.V30I1.10419. URL https://doi.org/10.1609/aaai.v30i1.10419.

Kareem Ahmed, Stefano Teso, Kai-Wei Chang, Guy Van den Broeck, and Antonio Vergari. Semantic Probabilistic Layers for Neuro-Symbolic Learning. In *NeurIPS*, 2022a.

Kareem Ahmed, Stefano Teso, Kai-Wei Chang, Guy Van den Broeck, and Antonio Vergari. Semantic probabilistic layers for neuro-symbolic learning. *Advances in Neural Information Processing Systems*, 35:29944–29959, 2022b.

Kareem Ahmed, Kai-Wei Chang, and Guy Van den Broeck. A pseudo-semantic loss for autoregressive models with logical constraints. In Alice Oh, Tristan Naumann, Amir Globerson, Kate Saenko, Moritz Hardt, and Sergey Levine, editors, *Advances in Neural Information Processing Systems 36: Annual Conference on Neural Information Processing Systems 2023, NeurIPS 2023, New Orleans, LA, USA, December 10 - 16, 2023*, 2023.

Nina Amenta, Dominique Attali, and Olivier Devillers. Complexity of delaunay triangulation for points on lower-dimensional polyhedra. In *Proceedings of the Eighteenth Annual ACM-SIAM Symposium on Discrete Algorithms*, SODA '07, page 11061113, USA, 2007. Society for Industrial and Applied Mathematics. ISBN 9780898716245.

Velleda Baldoni, Nicole Berline, Jesús A. De Loera, Matthias Köppe, and Michèle Vergne. How to integrate a polynomial over a simplex. *Math. Comput.*, 80:297–325, 2008. URL https://api.semanticscholar.org/CorpusID:569190.

Velleda Baldoni, Nicole Berline, Jesus De Loera, Matthias Köppe, and Michèle Vergne. How to integrate a polynomial over a simplex. *Mathematics of Computation*, 80 (273):297–325, 2011.

Velleda Baldoni, Nicole Berline, Jesús A De Loera, Brandon Dutra, Matthias Köppe, Stanislav Moreinis, Gregory Pinto, Michele Vergne, and Jianqiu Wu. A users guide for latte integrale v1. 7.2. *Optimization*, 22(2), 2014.

C. Bradford Barber, David P. Dobkin, and Hannu Huhdanpaa. The quickhull algorithm for convex hulls. *ACM Trans. Math. Softw.*, 22(4):469483, December 1996. ISSN 0098-3500. doi: 10.1145/235815.235821. URL https://doi.org/10.1145/235815.235821.

Clark W. Barrett, Roberto Sebastiani, Sanjit A. Seshia, and Cesare Tinelli. Satisfiability Modulo Theories. In *Handbook of Satisfiability*, volume 336, chapter 33, pages 1267–1329. IOS Press, 2nd edition, 2021.

Vaishak Belle, Andrea Passerini, and Guy Van den Broeck. Probabilistic inference in hybrid domains by weighted model integration. In Qiang Yang and Michael J. Wooldridge, editors, *Proceedings of the Twenty-Fourth International Joint Conference on Artificial Intelligence, IJCAI 2015, Buenos Aires, Argentina, July 25-31, 2015*, pages 2770–2776. AAAI Press, 2015. URL http://ijcai.org/Abstract/15/392.

Christian Jimenez Beltran, Antonio Vergari, Aretha L Teckentrup, and Konstantinos C Zygalakis. Galerkin meets laplace: Fast uncertainty estimation in neural pdes. In *ICLR 2024 Workshop on AI4DifferentialEquations In Science*, 2024.

Tom Beucler, Michael Pritchard, Pierre Gentine, and Stephan Rasp. Towards physically-consistent, data-driven models of convection. In *Igarss 2020-2020 ieee international geoscience and remote sensing symposium*, pages 3987–3990. IEEE, 2020.

Tom Beucler, Michael Pritchard, Stephan Rasp, Jordan Ott, Pierre Baldi, and Pierre Gentine. Enforcing analytic constraints in neural networks emulating physical systems. *Phys. Rev. Lett.*, 126: 098302, Mar 2021. doi: 10.1103/PhysRevLett.126.098302. URL https://link.aps.org/doi/10.1103/PhysRevLett.126.098302.

Christopher M Bishop. Mixture density networks. 1994.

Samuele Bortolotti, Emanuele Marconato, Tommaso Carraro, Paolo Morettin, Emile van Krieken, Antonio Vergari, Stefano Teso, and Andrea Passerini. A benchmark suite for systematically evaluating reasoning shortcuts. *NeurIPS Dataset and Benchmarks*, 2024.

Bernard Chazelle. An optimal convex hull algorithm in any fixed dimension. *Discrete Comput. Geom.*, 10 (4):377409, December 1993. ISSN 0179-5376. doi: 10.1007/BF02573985. URL https://doi.org/10.1007/BF02573985.

Yixin Cheng, Grigorios Chrysos, Markos Georgopoulos, and Volkan Cevher. Multilinear operator networks. In *The Twelfth International Conference on Learning Representations*, 2024.

Eric B Chin and N Sukumar. An efficient method to integrate polynomials over polytopes and curved solids. *Computer Aided Geometric Design*, 82:101914, 2020.

YooJung Choi, Antonio Vergari, and Guy Van den Broeck. Probabilistic circuits: A unifying framework for tractable probabilistic models. 2020.

Adnan Darwiche and Pierre Marquis. A knowledge compilation map. *Journal of Artificial Intelligence Research*, 17:229–264, 2002.

Luc De Raedt, Sebastijan Dumančić, Robin Manhaeve, and Giuseppe Marra. From statistical relational to neural-symbolic artificial intelligence. In *Proceedings of the Twenty-Ninth International Conference on International Joint Conferences on Artificial Intelligence*, pages 4943–4950, 2021.

Lennert De Smet and Pedro Zuidberg Dos Martires. A fast convoluted story: Scaling probabilistic inference for integer arithmetics. In *The Thirty-eighth Annual Conference on Neural Information Processing Systems*, 2024.

Lennert De Smet, Pedro Zuidberg Dos Martires, Robin Manhaeve, Giuseppe Marra, Angelika Kimmig, and Luc De Raedt. Neural probabilistic logic programming in discrete-continuous domains. In Robin J. Evans and Ilya Shpitser, editors, *Uncertainty in Artificial Intelligence, UAI 2023, July 31 - 4 August 2023, Pittsburgh, PA, USA*, volume 216 of *Proceedings of Machine Learning Research*, pages 529–538. PMLR, 2023a. URL https://proceedings.mlr.press/v216/de-smet23a.html.

Lennert De Smet, Emanuele Sansone, and Pedro Zuidberg Dos Martires. Differentiable sampling of categorical distributions using the catlog-derivative trick. *Advances in Neural Information Processing Systems*, 36, 2023b.

Aaron Defazio, Xingyu Yang, Harsh Mehta, Konstantin Mishchenko, Ahmed Khaled, and Ashok Cutkosky. The road less scheduled. *ArXiv*, abs/2405.15682, 2024. URL https://api.semanticscholar.org/CorpusID:270045085.

Michelangelo Diligenti, Marco Gori, and Claudio Saccà. Semantic-based regularization for learning and inference. *Artif. Intell.*, 244:143–165, 2017. doi: 10.1016/J.ARTINT.2015.08.011. URL https://doi.org/10.1016/j.artint.2015.08.011.

Pedro Zuidberg Dos Martires, Anton Dries, and Luc De Raedt. Exact and approximate weighted model integration with probability density functions using knowledge compilation. In *The Thirty-Third AAAI Conference on Artificial Intelligence, AAAI 2019, The Thirty-First Innovative Applications of Artificial Intelligence Conference, IAAI 2019, The Ninth AAAI Symposium on Educational Advances in Artificial Intelligence, EAAI 2019, Honolulu, Hawaii, USA, January 27 - February 1, 2019*, pages 7825–7833. AAAI Press, 2019. doi: 10.1609/AAAI.V33I01.33017825. URL https://doi.org/10.1609/aaai.v33i01.33017825.

Conor Durkan, Artur Bekasov, Iain Murray, and George Papamakarios. Neural spline flows. In Hanna M. Wallach, Hugo Larochelle, Alina Beygelzimer, Florence d'Alché-Buc, Emily B. Fox, and Roman Garnett, editors, *Advances in Neural Information Processing Systems 32: Annual Conference on Neural Information Processing Systems 2019, NeurIPS 2019, December 8-14, 2019, Vancouver, BC, Canada*, pages 7509–7520, 2019. URL https://proceedings.neurips.cc/paper/2019/hash/7ac71d433f282034e088473244df8c02-Abstract.html.

Marc Fischer, Mislav Balunovic, Dana Drachsler-Cohen, Timon Gehr, Ce Zhang, and Martin T. Vechev. DL2: training and querying neural networks with logic. In Kamalika Chaudhuri and Ruslan Salakhutdinov, editors, *Proceedings of the 36th International Conference on Machine Learning, ICML 2019, 9-15 June 2019, Long Beach, California, USA*, volume 97 of *Proceedings of Machine Learning Research*, pages 1931–1941. PMLR, 2019. URL http://proceedings.mlr.press/v97/fischer19a.html.

A Garcez, M Gori, LC Lamb, L Serafini, M Spranger, and SN Tran. Neural-symbolic computing: An effective methodology for principled integration of machine learning and reasoning. *Journal of Applied Logics*, 6(4): 611–632, 2019.

Artur dAvila Garcez, Sebastian Bader, Howard Bowman, Luis C Lamb, Leo de Penning, BV Illuminoo, Hoifung Poon, and COPPE Gerson Zaverucha. Neural-symbolic learning and reasoning: A survey and interpretation. *Neuro-Symbolic Artificial Intelligence: The State of the Art*, 342:1, 2022.

Eleonora Giunchiglia and Thomas Lukasiewicz. Coherent hierarchical multi-label classification networks. *NeurIPS*, 2020.

Eleonora Giunchiglia, Mihaela Cătălina Stoian, Salman Khan, Fabio Cuzzolin, and Thomas Lukasiewicz. Road-r: The autonomous driving dataset with logical requirements. *Machine Learning*, pages 1–31, 2023.

Xavier Glorot, Antoine Bordes, and Yoshua Bengio. Deep sparse rectifier neural networks. In Geoffrey J. Gordon, David B. Dunson, and Miroslav Dudík, editors, *Proceedings of the Fourteenth International Conference on Artificial Intelligence and Statistics, AISTATS 2011, Fort Lauderdale, USA, April 11-13, 2011*, volume 15 of *JMLR Proceedings*, pages 315–323. JMLR.org, 2011. URL http://proceedings.mlr.press/v15/glorot11a/glorot11a.pdf.

Kshitij Goyal, Sebastijan Dumancic, and Hendrik Blockeel. Deepsade: Learning neural networks that guarantee domain constraint satisfaction. In Michael J. Wooldridge,

Jennifer G. Dy, and Sriraam Natarajan, editors, *Thirty-Eighth AAAI Conference on Artificial Intelligence, AAAI 2024, Thirty-Sixth Conference on Innovative Applications of Artificial Intelligence, IAAI 2024, Fourteenth Symposium on Educational Advances in Artificial Intelligence, EAAI 2014, February 20-27, 2024, Vancouver, Canada*, pages 12199–12207. AAAI Press, 2024. doi: 10.1609/AAAI.V38I11.29109. URL https://doi.org/10.1609/aaai.v38i11.29109.

Andreas Grivas, Antonio Vergari, and Adam Lopez. Taming the sigmoid bottleneck: Provably argmaxable sparse multi-label classification. In *Proceedings of the AAAI Conference on Artificial Intelligence*, volume 38, pages 12208–12216, 2024.

Axel Grundmann and H. M. Möller. Invariant integration formulas for the n-simplex by combinatorial methods. *SIAM Journal on Numerical Analysis*, 15(2):282–290, 1978. doi: 10.1137/0715019. URL https://doi.org/10.1137/0715019.

Paula Harder, Alex Hernández-García, Venkatesh Ramesh, Qidong Yang, Prasanna Sattegeri, Daniela Szwarcman, Campbell D. Watson, and David Rolnick. Hard-constrained deep learning for climate downscaling. *J. Mach. Learn. Res.*, 24:365:1–365:40, 2023. URL http://jmlr.org/papers/v24/23-0158.html.

Geoffrey E Hinton. Training products of experts by minimizing contrastive divergence. *Neural computation*, 14 (8):1771–1800, 2002.

Nick Hoernle, Rafael Michael Karampatsis, Vaishak Belle, and Kobi Gal. Multiplexnet: Towards fully satisfied logical constraints in neural networks. In *AAAI*, 2022.

Volker Kaibel and Marc E. Pfetsch. Some algorithmic problems in polytope theory, 2002. URL https://arxiv.org/abs/math/0202204.

Diederik P. Kingma and Jimmy Ba. Adam: A method for stochastic optimization. In Yoshua Bengio and Yann LeCun, editors, *3rd International Conference on Learning Representations, ICLR 2015, San Diego, CA, USA, May 7-9, 2015, Conference Track Proceedings*, 2015a. URL http://arxiv.org/abs/1412.6980.

Diederik P. Kingma and Jimmy Ba. Adam: A method for stochastic optimization. In Yoshua Bengio and Yann LeCun, editors, *3rd International Conference on Learning Representations, ICLR 2015, San Diego, CA, USA, May 7-9, 2015, Conference Track Proceedings*, 2015b. URL http://arxiv.org/abs/1412.6980.

Samuel Kolb, Martin Mladenov, Scott Sanner, Vaishak Belle, and Kristian Kersting. Efficient symbolic integration for probabilistic inference. In Jérôme Lang, editor, *Proceedings of the Twenty-Seventh International Joint Conference on Artificial Intelligence, IJCAI 2018, July 13-19, 2018, Stockholm, Sweden*, pages 5031–5037. ijcai.org, 2018a. doi: 10.24963/IJCAI.2018/698. URL https://doi.org/10.24963/ijcai.2018/698.

Samuel Kolb, Stefano Teso, Andrea Passerini, and Luc De Raedt. Learning SMT(LRA) constraints using SMT solvers. In Jérôme Lang, editor, *Proceedings of the Twenty-Seventh International Joint Conference on Artificial Intelligence, IJCAI 2018, July 13-19, 2018, Stockholm, Sweden*, pages 2333–2340. ijcai.org, 2018b. doi: 10.24963/IJCAI.2018/323. URL https://doi.org/10.24963/ijcai.2018/323.

Zongyi Li, Nikola Kovachki, Kamyar Azizzadenesheli, Burigede Liu, Kaushik Bhattacharya, Andrew Stuart, and Anima Anandkumar. Fourier neural operator for parametric partial differential equations. *arXiv preprint arXiv:2010.08895*, 2020.

Dong C Liu and Jorge Nocedal. On the limited memory bfgs method for large scale optimization. *Mathematical programming*, 45(1):503–528, 1989.

Lorenzo Loconte and Antonio Vergari. On faster marginalization with squared circuits via orthonormalization. In *CoLoRAI - The AAAI25 Workshop on Connecting Low-rank Representations in AI*, 2025. URL https://openreview.net/forum?id=WTRBDY9m3n.

Lorenzo Loconte, M. Sladek Aleksanteri, Stefan Mengel, Martin Trapp, Arno Solin, Nicolas Gillis, and Antonio Vergari. Subtractive mixture models via squaring: Representation and learning. In *The Twelfth International Conference on Learning Representations*, 2024. URL https://openreview.net/forum?id=xIHi5nxu9P.

Lorenzo Loconte, Antonio Mari, Gennaro Gala, Robert Peharz, Cassio de Campos, Erik Quaeghebeur, Gennaro Vessio, and Antonio Vergari. What is the relationship between tensor factorizations and circuits (and how can we exploit it)? *Transactions of Machine Learning Research*, 2025a. URL https://openreview.net/forum?id=Y7dRmpGiHj.

Lorenzo Loconte, Stefan Mengel, and Antonio Vergari. Sum of squares circuits. In *The 39th Annual AAAI Conference on Artificial Intelligence*, 2025b.

Lu Lu, Raphael Pestourie, Wenjie Yao, Zhicheng Wang, Francesc Verdugo, and Steven G Johnson. Physics-informed neural networks with hard constraints for inverse design. *SIAM Journal on Scientific Computing*, 43 (6):B1105–B1132, 2021.

Robin Manhaeve, Sebastijan Dumancic, Angelika Kimmig, Thomas Demeester, and Luc De Raedt. DeepProbLog:

Neural Probabilistic Logic Programming. *NeurIPS*, 2018.

Robin Manhaeve, Sebastijan Dumancic, Angelika Kimmig, Thomas Demeester, and Luc De Raedt. Neural probabilistic logic programming in deepproblog. *Artif. Intell.*, 298:103504, 2021. doi: 10.1016/J.ARTINT.2021.103504. URL https://doi.org/10.1016/j.artint.2021.103504.

Emanuele Marconato, Stefano Teso, Antonio Vergari, and Andrea Passerini. Not all neuro-symbolic concepts are created equal: Analysis and mitigation of reasoning shortcuts. In *NeurIPS*, 2023.

Emanuele Marconato, Samuele Bortolotti, Emile van Krieken, Antonio Vergari, Andrea Passerini, and Stefano Teso. BEARS Make Neuro-Symbolic Models Aware of their Reasoning Shortcuts. *Uncertainty in AI*, 2024.

Giuseppe Marra, Sebastijan Dumancic, Robin Manhaeve, and Luc De Raedt. From statistical relational to neurosymbolic artificial intelligence: A survey. *Artif. Intell.*, 328:104062, 2024. doi: 10.1016/J.ARTINT.2023.104062. URL https://doi.org/10.1016/j.artint.2023.104062.

Aaron Meurer, Christopher P. Smith, Mateusz Paprocki, Ondřej Čertík, Sergey B. Kirpichev, Matthew Rocklin, AMiT Kumar, Sergiu Ivanov, Jason K. Moore, Sartaj Singh, Thilina Rathnayake, Sean Vig, Brian E. Granger, Richard P. Muller, Francesco Bonazzi, Harsh Gupta, Shivam Vats, Fredrik Johansson, Fabian Pedregosa, Matthew J. Curry, Andy R. Terrel, Štěpán Roučka, Ashutosh Saboo, Isuru Fernando, Sumith Kulal, Robert Cimrman, and Anthony Scopatz. Sympy: symbolic computing in python. *PeerJ Computer Science*, 3:e103, January 2017a. ISSN 2376-5992. doi: 10.7717/peerj-cs.103. URL https://doi.org/10.7717/peerj-cs.103.

Aaron Meurer, Christopher P. Smith, Mateusz Paprocki, Ondřej Čertík, Sergey B. Kirpichev, Matthew Rocklin, AMiT Kumar, Sergiu Ivanov, Jason K. Moore, Sartaj Singh, Thilina Rathnayake, Sean Vig, Brian E. Granger, Richard P. Muller, Francesco Bonazzi, Harsh Gupta, Shivam Vats, Fredrik Johansson, Fabian Pedregosa, Matthew J. Curry, Andy R. Terrel, Štěpán Roučka, Ashutosh Saboo, Isuru Fernando, Sumith Kulal, Robert Cimrman, and Anthony Scopatz. Sympy: symbolic computing in python. *PeerJ Computer Science*, 3:e103, January 2017b. ISSN 2376-5992. doi: 10.7717/peerj-cs.103. URL https://doi.org/10.7717/peerj-cs.103.

Paolo Morettin, Andrea Passerini, and Roberto Sebastiani. Efficient weighted model integration via smt-based predicate abstraction. In Carles Sierra, editor, *Proceedings of the Twenty-Sixth International Joint Conference on Artificial Intelligence, IJCAI 2017, Melbourne, Australia, August 19-25, 2017*, pages 720–728. ijcai.org, 2017. doi: 10.24963/IJCAI.2017/100. URL https://doi.org/10.24963/ijcai.2017/100.

Paolo Morettin, Samuel Kolb, Stefano Teso, and Andrea Passerini. Learning weighted model integration distributions. In *The Thirty-Fourth AAAI Conference on Artificial Intelligence, AAAI 2020, The Thirty-Second Innovative Applications of Artificial Intelligence Conference, IAAI 2020, The Tenth AAAI Symposium on Educational Advances in Artificial Intelligence, EAAI 2020, New York, NY, USA, February 7-12, 2020*, pages 5224–5231. AAAI Press, 2020. doi: 10.1609/AAAI.V34I04.5967. URL https://doi.org/10.1609/aaai.v34i04.5967.

Paolo Morettin, Pedro Zuidberg Dos Martires, Samuel Kolb, and Andrea Passerini. Hybrid probabilistic inference with logical and algebraic constraints: a survey. In Zhi-Hua Zhou, editor, *Proceedings of the Thirtieth International Joint Conference on Artificial Intelligence, IJCAI 2021, Virtual Event / Montreal, Canada, 19-27 August 2021*, pages 4533–4542. ijcai.org, 2021. doi: 10.24963/IJCAI.2021/617. URL https://doi.org/10.24963/ijcai.2021/617.

Paolo Morettin, Andrea Passerini, and Roberto Sebastiani. A unified framework for probabilistic verification of ai systems via weighted model integration. *arXiv preprint arXiv:2402.04892*, 2024.

Adam Paszke, Sam Gross, Francisco Massa, Adam Lerer, James Bradbury, Gregory Chanan, Trevor Killeen, Zeming Lin, Natalia Gimelshein, Luca Antiga, Alban Desmaison, Andreas Köpf, Edward Z. Yang, Zach DeVito, Martin Raison, Alykhan Tejani, Sasank Chilamkurthy, Benoit Steiner, Lu Fang, Junjie Bai, and Soumith Chintala. Pytorch: An imperative style, high-performance deep learning library. *CoRR*, abs/1912.01703, 2019a. URL http://arxiv.org/abs/1912.01703.

Adam Paszke, Sam Gross, Francisco Massa, Adam Lerer, James Bradbury, Gregory Chanan, Trevor Killeen, Zeming Lin, Natalia Gimelshein, Luca Antiga, et al. Pytorch: An imperative style, high-performance deep learning library. *Advances in neural information processing systems*, 32, 2019b.

Samuel Pfrommer, Tanmay Gautam, Alec Zhou, and Somayeh Sojoudi. Safe reinforcement learning with chance-constrained model predictive control. In Roya Firoozi, Negar Mehr, Esen Yel, Rika Antonova, Jeannette Bohg, Mac Schwager, and Mykel J. Kochenderfer, editors, *Learning for Dynamics and Control Conference, L4DC 2022, 23-24 June 2022, Stanford University, Stanford, CA, USA*, volume 168 of *Proceedings of Machine Learning Research*, pages 291–303.

PMLR, 2022. URL https://proceedings.mlr.press/v168/pfrommer22a.html.

Maziar Raissi, Paris Perdikaris, and George E Karniadakis. Physics-informed neural networks: A deep learning framework for solving forward and inverse problems involving nonlinear partial differential equations. *Journal of Computational physics*, 378:686–707, 2019.

Kai Ren, Colin Chen, Hyeontae Sung, Heejin Ahn, Ian M. Mitchell, and Maryam Kamgarpour. Safe chance-constrained model predictive control under gaussian mixture model uncertainty. *CoRR*, abs/2401.03799, 2024. doi: 10.48550/ARXIV.2401.03799. URL https://doi.org/10.48550/arXiv.2401.03799.

Alexandre Robicquet, Amir Sadeghian, Alexandre Alahi, and Silvio Savarese. Learning social etiquette: Human trajectory understanding in crowded scenes. In Bastian Leibe, Jiri Matas, Nicu Sebe, and Max Welling, editors, *Computer Vision - ECCV 2016 - 14th European Conference, Amsterdam, The Netherlands, October 11-14, 2016, Proceedings, Part VIII*, volume 9912 of *Lecture Notes in Computer Science*, pages 549–565. Springer, 2016. doi: 10.1007/978-3-319-46484-8_33. URL https://doi.org/10.1007/978-3-319-46484-8_33.

Raimund Seidel. The upper bound theorem for polytopes: an easy proof of its asymptotic version. *Computational Geometry*, 5(2):115–116, 1995. ISSN 0925-7721. doi: https://doi.org/10.1016/0925-7721(95)00013-Y. URL https://www.sciencedirect.com/science/article/pii/092577219500013Y.

Philip W Smith. A practical guide to splines (carl de boor). *SIAM Review*, 22(4):520, 1980.

Giuseppe Spallitta, Gabriele Masina, Paolo Morettin, Andrea Passerini, and Roberto Sebastiani. Smt-based weighted model integration with structure awareness. In James Cussens and Kun Zhang, editors, *Uncertainty in Artificial Intelligence, Proceedings of the Thirty-Eighth Conference on Uncertainty in Artificial Intelligence, UAI 2022, 1-5 August 2022, Eindhoven, The Netherlands*, volume 180 of *Proceedings of Machine Learning Research*, pages 1876–1885. PMLR, 2022. URL https://proceedings.mlr.press/v180/spallitta22a.html.

Giuseppe Spallitta, Gabriele Masina, Paolo Morettin, Andrea Passerini, and Roberto Sebastiani. Enhancing smt-based weighted model integration by structure awareness. *Artif. Intell.*, 328:104067, 2024. doi: 10.1016/J.ARTINT.2024.104067. URL https://doi.org/10.1016/j.artint.2024.104067.

Russell Stewart and Stefano Ermon. Label-free supervision of neural networks with physics and domain knowledge. In Satinder Singh and Shaul Markovitch, editors, *Proceedings of the Thirty-First AAAI Conference on Artificial Intelligence, February 4-9, 2017, San Francisco, California, USA*, pages 2576–2582. AAAI Press, 2017. doi: 10.1609/AAAI.V31I1.10934. URL https://doi.org/10.1609/aaai.v31i1.10934.

Mihaela C. Stoian, Salijona Dyrmishi, Maxime Cordy, Thomas Lukasiewicz, and Eleonora Giunchiglia. How realistic is your synthetic data? constraining deep generative models for tabular data. In *The Twelfth International Conference on Learning Representations, ICLR 2024, Vienna, Austria, May 7-11, 2024*. OpenReview.net, 2024a. URL https://openreview.net/forum?id=tBROYsEz9G.

Mihaela C. Stoian, Alex Tatomir, Thomas Lukasiewicz, and Eleonora Giunchiglia. Pishield: A pytorch package for learning with requirements. In *Proceedings of the Thirty-Third International Joint Conference on Artificial Intelligence, IJCAI 2024, Jeju, South Korea, August 3-9, 2024*, pages 8805–8809. ijcai.org, 2024b. URL https://www.ijcai.org/proceedings/2024/1037.

Mihaela Catalina Stoian and Eleonora Giunchiglia. Beyond the convexity assumption: Realistic tabular data generation under quantifier-free real linear constraints. *CoRR*, abs/2502.18237, 2025. doi: 10.48550/ARXIV.2502.18237. URL https://doi.org/10.48550/arXiv.2502.18237.

Mihaela Catalina Stoian, Salijona Dyrmishi, Maxime Cordy, Thomas Lukasiewicz, and Eleonora Giunchiglia. How realistic is your synthetic data? constraining deep generative models for tabular data. *CoRR*, abs/2402.04823, 2024c. doi: 10.48550/ARXIV.2402.04823. URL https://doi.org/10.48550/arXiv.2402.04823.

Emile van Krieken, Pasquale Minervini, Edoardo M. Ponti, and Antonio Vergari. On the independence assumption in neurosymbolic learning. In *International Conference on Machine Learning*. PMLR, 2024.

Antonio Vergari, YooJung Choi, Anji Liu, Stefano Teso, and Guy Van den Broeck. A compositional atlas of tractable circuit operations for probabilistic inference. *Advances in Neural Information Processing Systems*, 34, 2021.

Jared Willard, Xiaowei Jia, Shaoming Xu, Michael Steinbach, and Vipin Kumar. Integrating physics-based modeling with machine learning: A survey. *arXiv preprint arXiv:2003.04919*, 1(1):1–34, 2020.

Yu-Huan Wu, Yun Liu, Xin Zhan, and Ming-Ming Cheng. P2T: pyramid pooling transformer for scene understanding. *IEEE Trans. Pattern Anal. Mach. Intell.*, 45 (11):12760–12771, 2023. doi: 10.1109/TPAMI.2022.3202765. URL https://doi.org/10.1109/TPAMI.2022.3202765.

Jingyi Xu, Zilu Zhang, Tal Friedman, Yitao Liang, and Guy Van den Broeck. A semantic loss function for deep learning with symbolic knowledge. In Jennifer G. Dy and Andreas Krause, editors, *Proceedings of the 35th International Conference on Machine Learning, ICML 2018, Stockholmsmässan, Stockholm, Sweden, July 10-15, 2018*, volume 80 of *Proceedings of Machine Learning Research*, pages 5498–5507. PMLR, 2018. URL http://proceedings.mlr.press/v80/xu18h.html.

Yiran Xu, Xiaoyin Yang, Lihang Gong, Hsuan-Chu Lin, Tz-Ying Wu, Yunsheng Li, and Nuno Vasconcelos. Explainable object-induced action decision for autonomous vehicles. In *IEEE/CVF Conference on Computer Vision and Pattern Recognition (CVPR)*, June 2020.

Seungil You, David Ding, Kevin Robert Canini, Jan Pfeifer, and Maya R. Gupta. Deep lattice networks and partial monotonic functions. In Isabelle Guyon, Ulrike von Luxburg, Samy Bengio, Hanna M. Wallach, Rob Fergus, S. V. N. Vishwanathan, and Roman Garnett, editors, *Advances in Neural Information Processing Systems 30: Annual Conference on Neural Information Processing Systems 2017, December 4-9, 2017, Long Beach, CA, USA*, pages 2981–2989, 2017. URL https://proceedings.neurips.cc/paper/2017/hash/464d828b85b0bed98e80ade0a5c43b0f-Abstract.html.

Manzil Zaheer, Satwik Kottur, Siamak Ravanbakhsh, Barnabás Póczos, Ruslan Salakhutdinov, and Alexander J. Smola. Deep sets. In Isabelle Guyon, Ulrike von Luxburg, Samy Bengio, Hanna M. Wallach, Rob Fergus, S. V. N. Vishwanathan, and Roman Garnett, editors, *Advances in Neural Information Processing Systems 30: Annual Conference on Neural Information Processing Systems 2017, December 4-9, 2017, Long Beach, CA, USA*, pages 3391–3401, 2017. URL https://proceedings.neurips.cc/paper/2017/hash/f22e4747da1aa27e363d86d40ff442fe-Abstract.html.

Zhe Zeng and Guy Van den Broeck. Efficient search-based weighted model integration. In Amir Globerson and Ricardo Silva, editors, *Proceedings of the Thirty-Fifth Conference on Uncertainty in Artificial Intelligence, UAI 2019, Tel Aviv, Israel, July 22-25, 2019*, volume 115 of *Proceedings of Machine Learning Research*, pages 175–185. AUAI Press, 2019. URL http://proceedings.mlr.press/v115/zeng20a.html.

Zhe Zeng and Guy Van den Broeck. Collapsed inference for bayesian deep learning. *Advances in Neural Information Processing Systems*, 36:78394–78411, 2023.

Zhe Zeng, Paolo Morettin, Fanqi Yan, Antonio Vergari, and Guy Van den Broeck. Probabilistic inference with algebraic constraints: Theoretical limits and practical approximations. *Advances in Neural Information Processing Systems*, 33:11564–11575, 2020a.

Zhe Zeng, Paolo Morettin, Fanqi Yan, Antonio Vergari, and Guy Van den Broeck. Scaling up hybrid probabilistic inference with logical and arithmetic constraints via message passing. In *International Conference on Machine Learning*, pages 10990–11000. PMLR, 2020b.

Zhe Zeng, Paolo Morettin, Fanqi Yan, Antonio Vergari, Andrea Passerini, Guy Van den Broeck, et al. Is parameter learning via weighted model integration tractable? In *4th Workshop on Tractable Probabilistic Modeling*. UAI, 2021.

A Probabilistic Neuro-symbolic Layer for Algebraic Constraint Satisfaction (Supplementary Material)

Leander Kurscheidt[1] **Paolo Morettin**[2] **Roberto Sebastiani**[2] **Andrea Passerini**[2] **Antonio Vergari**[1]

[1]School of Informatics, University of Edinburgh, UK
[2]DiSI, University of Trento, Italy

A BACKGROUND ON WEIGHTED MODEL INTEGRATION

The task of marginalizing over a distribution defined by a density over SMT($\mathcal{LRA}$) constraints is known as *weighted model integration* [Belle et al., 2015]. WMI generalizes weighted model counting (WMC), i.e. the task of summing over the models of a propositional logic formula, to the hybrid logical/continuous domain. In WMC, each satisfying truth assignment μ is a model, whose weight typically factorizes over the literals:

$$\mathsf{WMC}(\phi, w) = \sum_{\mu \models \phi} \prod_{\ell \in \mu} w(\ell)$$

In WMI, each μ induces a convex (and disjoint) subregion of ϕ. For $\mathsf{WMI}(\phi, w)$ to be finite, ϕ must encode a closed region. In those cases, each μ induces a convex polytope containing infinitely many models, i.e. assignments $\boldsymbol{x} \models \mu$. The weight function w can be interpreted in probabilistic terms as an unnormalized density over $\mathbf{X}$. Then, obtaining the weight of each μ additionally requires integrating w over those models:

$$\mathsf{WMI}(\phi, w) = \underbrace{\sum_{\mu \models \phi}}_{(1)} \underbrace{\int w(\boldsymbol{x}) \mathbb{1}\{\boldsymbol{x} \models \mu\} \; d\mathbf{X}}_{(2)} \tag{4}$$

Computing WMI requires solving two subtasks:

(1) *enumerating* all the $\mu \models \phi$;
(2) *integrating* w inside each μ.

For our purposes, WMI exactly corresponds to the problem of computing the normalizing constant in Eq. PAL:

$$\int w(\boldsymbol{x}) \mathbb{1}\{\boldsymbol{x} \models \phi\} \; d\mathbf{X} = \sum_{\mu \models \phi} \int w(\boldsymbol{x}) \mathbb{1}\{\boldsymbol{x} \models \mu\} \; d\mathbf{X} \tag{5}$$

Partial enumeration. In `GASP!`, we solve Eq. 5 by decomposing the integral into convex polytopes first and then further decomposing each polytope into simplices. Clearly, obtaining a compact decomposition of ϕ into disjoint convex regions is paramount for reducing the size of the computational graph. In this work, we leverage the enumeration procedure of SAE4WMI [Spallitta et al., 2024] for solving subtask (1). SAE4WMI builds upon a line of work that leverages advanced SMT techniques [Morettin et al., 2017, Spallitta et al., 2022] for minimizing the number of integrations. A key idea of these solver is the enumeration of *partial* (as opposed to *total*) satisfying truth assignments. For the purpose of WMI, the set of satisfying truth assignments $TA(\phi)$ must be complete ($\bigvee_{\mu \in TA(\phi)} \mu \equiv \phi$) and it must contain mutually exclusive/disjoint elements ($\forall i \neq j \; . \; \mu_i \wedge \mu_j \models \bot$). As opposed to total assignments, partial assignments are not required to map every inequality of ϕ to $\{True, False\}$.

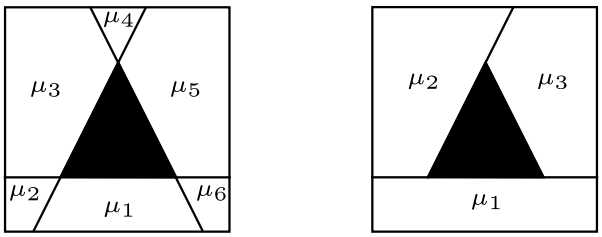

Figure 10: A decomposition of the non-convex constraint in our running example with total (*left*) vs. partial (*right*) satisfying truth assignments.

It is easy to show that the latter can exponentially reduce the number of partitions of ϕ by considering a disjunction among N atomic formulas: $\phi = \bigvee_{i=1}^{N} A_i$. While the size of the set of total satisfying truth assignment is $2^N - 1$, we can fully characterize the formula with N disjoint partial assignments $\phi = \bigvee_{i=1}^{N} \mu_i$, where:

$$\begin{aligned}
&\mu_1 = A_1 \\
&\mu_2 = \neg A_1 \wedge A_2 \\
&\mu_3 = \neg A_1 \wedge \neg A_2 \wedge A_3 \\
&... \\
&\mu_N = \neg A_1 \wedge \neg A_2 \wedge ... \wedge \neg A_{N-1} \wedge A_N
\end{aligned}$$

The benefits of enumerating partial truth assignments is evident even in our lower dimensional example, as depicted in Figure 10.

B TRAINING AND PARAMETRIZING POLYNOMIALS

We tested `PAL` with two kinds of polynomial density: single polynomials and cubic, hermite splines.

As expressiveness is tied to increasing the total degree, the former might be difficult to employ in fitting very complex distributions. We turned to the latter in the Stanford Drone use cases, partitioning the overall density into equally-sized bins, each encoded as the product of squared univariate splines. Furthermore, we consider a mixture of the parametric form above. The resulting parametric form is both stable to train and expressive, while also leveraging the amortization capabilities of `GASP!` for each bin.

We will first specify the exact re-parametrization and methods we used for both raw polynomials and splines, and then detail the loss.

B.1 POLYNOMIALS

We experienced some difficulty during training when trying to directly predict coefficients of single polynomials, due to the different scale-sensitivity of the monomials. We tackled this issue for the N-pointed star experiments in by adding a re-parametrization layer in front of the polynomial. Let $I(\mathbf{\Lambda}) = \sum_i \sum_j \mathbf{\Lambda}_i \mathbf{\Lambda}_j \eta_{ij}$ be the integrated, squared polynomial. Then our re-parametrization is the following:

$$r(z_i) = \texttt{sign}(z_i) \frac{\sqrt{z_i + d'} - \sqrt{d'}}{\sqrt{\eta_{ii}}}$$

with $d' = 0.1$. This dampens the impact of coefficients of high-degree monomials, as they are often associated with large η_{ii}.

Additionally, before training, we initialize the magnitude of the output of our last layer by fitting a constant scalar per dimension using L-BFGS [Liu and Nocedal, 1989] over the first 1000 training samples.

While, with these methods, we are able to train `PAL` for a single, high-degree polynomial in a stable manner, we want to stress that they are not needed for the spline-parametrization.

B.2 POLYNOMIAL SPLINES

We use univariate, cubic, Hermite splines [Smith, 1980], which we then square to guarantee non-negativity and multiply to create multivariate splines.

Each spline is specified by the value and derivative at the knots. In order to evaluate and integrate, we create the explicit polynomial. We will now focus on a specific bin $[k_i, k_{i+1}]$. We view the spline just as a re-parametrization of a polynomial and compute the coefficients explicitly, in order to plug into the our framework to quickly compute the integral $I(\boldsymbol{\lambda})$. In comparison to the usual way to construct splines, in which the spline is constructed on the standard-bin $[0, 1]$, we have to account for scale. We therefore construct the parameters corresponding to the polynomial on the $[0, k_{i+1} - k_i]$ and shift the monomials m via $m'(x) = m(x - k_{i+1})$ before handing them to `GASP!`. The flexibility of shifting via a coordinate transform, instead of transforming the parameters of the polynomial, which is numerically instable, shows the adaptability and versatility of `GASP!`. The computed parameters of `GASP!` belong to the polynomial on $[0, k_{i+1} - k_i]$ per bin, and are numerically significantly more stable to evaluate than explicitly constructing the parameters of the shifted polynomial on $[k_i, k_{i+1}]$.

Given k_i and k_{i+1}, we compute the parameters as follows, which is a straightforward adaptation of the standard construction on $[0, 1]$.

First, we construct the parameters $a + b \cdot x + c \cdot x^2 + d \cdot x^3$ on $[0, 1]$. With v_i, v_{i+1} we denote the value and v'_i, v'_{i+1} the derivative:

$$
\begin{aligned}
a &= v_i \\
b &= v'_i \\
c &= 3 \cdot (v_{i+1} - v_i) - 2 \cdot v'_i - v'_{i+1} \\
d &= 2 \cdot (v_i - v_{i+1}) + v'_i + v'_{i+1}
\end{aligned}
$$

We then scale the polynomial by transforming the parameters. Let $\Delta = (k_{i+1} - k_i)$, then:

$$
\begin{aligned}
a' &= a \\
b' &= b \cdot (1/\Delta) \\
c' &= c \cdot (1/\Delta^2) \\
d' &= c \cdot (1/\Delta^3)
\end{aligned}
$$

These are the coefficients corresponding to the unsquared polynomial. The squared polynomial (of degree 6) is then just the combination of these parameters with itself, just as the multiplication of two splines is a combination of the respective parameters. Additionally, we take a mixture of these splines. These form $\boldsymbol{\lambda}$.

We integrate by enumerating the bins, shifting the monomials, and then obtain the coefficients for $I(\boldsymbol{\lambda})$ and during training, we view the piecewise spline as a re-parametrization layer that transforms the output of the neural network, so value and derivative at the knots, into the coefficients of the polynomial.

B.3 LOSS

For `PAL`, we minimize the following loss:

$$
l(\boldsymbol{x}^{[1:b]}, \boldsymbol{y}^{[1:b]}) = (-1) * \underbrace{\sum_b \log p_{\boldsymbol{\Theta}}(\boldsymbol{y}^{(b)} \mid \boldsymbol{x}^{(b)})}_{\text{constrained log-likelihood}} + \underbrace{\sum_b \mathbb{1}\{\log i_b \geq 10\} \, (\log i_b - 10)^2}_{\text{penalty on too large values of } I(\boldsymbol{\lambda} = f_\psi(\boldsymbol{x}^{(b)}))} \tag{6}
$$

with $i_b = I(\boldsymbol{\lambda} = f_\psi(\boldsymbol{x}^{(b)}))$. This loss biases the neural network towards more numerically-stable range of integral-values. Due to the scale-invariance, this does not influence the expressivity and only influences numerical stability. Although we

use it for both raw polynomials and splines, it's main use is to stabilize training of raw polynomials as the splines are inherently easier to train.

C GASP!

C.1 HANDLING THE SYMBOLIC POLYNOMIAL

We start with an symbolic polynomial $q(\boldsymbol{y}, \boldsymbol{\lambda})$ of the form:

$$\begin{aligned} q(\boldsymbol{y}, \boldsymbol{\lambda}) &= \sum_i \lambda_i \prod_j y_j^{\alpha_{ij}} \\ &= \sum_i \lambda_i m_i(\boldsymbol{y}) \end{aligned}$$

where $m_i(\boldsymbol{y})$ denotes the ith monomial. This induces the vector-valued version of the polynomial:

$$\vec{v}_q(\boldsymbol{y}) = \begin{pmatrix} m_{i_1}(\boldsymbol{y}) \\ m_{i_2}(\boldsymbol{y}) \\ \vdots \\ m_{i_n}(\boldsymbol{y}) \end{pmatrix}$$

This function $\vec{v}_q$ is completely independent of $\boldsymbol{\lambda}$, and can be directly plugged into `GASP!` to obtain the integral over each monomial $m_i(\boldsymbol{y})$. This construction also makes it straightforward to parallelize using existing frameworks like PyTorch [Paszke et al., 2019b].

We therefore use the following algorithm for the symbolic integration using `GASP!`:

Algorithm 3 SymbolicIntegral$(q, \mathbf{H})$

Input Polynomial $q(\boldsymbol{y}, \boldsymbol{\lambda})$, Polytope $\mathbf{H}$
Output $I(\boldsymbol{\lambda}) = \int_{\mathbf{H}} q(\boldsymbol{y}, \boldsymbol{\lambda}) d\mathbf{Y} = \sum \lambda_i \eta_i$

1: $\vec{v}_q \leftarrow$ ToVectorValued(q)
2: $\eta \leftarrow$ GASP!$(\vec{v}_q, \mathbf{H})$ {see Algorithm 1}
3: **return** $\boldsymbol{\lambda} \rightarrow \mathsf{I}(\boldsymbol{\lambda}; \eta)$ {a function (computational graph) that maps $\boldsymbol{\lambda}$ to the integral $\mathsf{I}(\boldsymbol{\lambda}; \eta)$ }

C.2 EXTENDED COMPLEXITY ANALYSIS OF GASP!

C.2.1 Detailed Analysis of GASP!

We will now detail the algorithm used to solve the non-symbolic integration problem over the convex polytope $\mathbf{H}$: $\int_{\mathbf{H}} q(\boldsymbol{y}) d\mathbf{Y}$, where q denotes a polynomial that is only over $\boldsymbol{y}$ (not $\boldsymbol{y}$ and $\boldsymbol{\lambda}$).

The main entry-point for `GASP!` is Algorithm 1, which takes a polynomial q and a convex polytope $\mathbf{H}$ in $\mathcal{H}$-description, so defined via $\mathbf{H} = \{\boldsymbol{y} | \mathbf{A}\boldsymbol{y} \leq \mathbf{b}\}$, and returns the integral $\int_{\mathbf{H}} q(\boldsymbol{y}) d\mathbf{Y}$. Being based on a cubature integration-formula over the unit-simplex, the first step is first querying the total degree of q and then creating the cubature points and weight (L2, Algorithm 1). The total number of points and weights depend on the degree, but are exact for any polynomial up to the respective degree. The cubature points and weights follow theorem 4 of Grundmann and Möller [1978], also provided in Algorithm 4. Given a polynomial of total degree d and dimension n, enumerating the points has a complexity of $\mathcal{O}(r \cdot \binom{r+n-1}{n-1})$ for $r = \lceil \frac{d}{2} - 1 \rceil$. In practice, this is done on the CPU and re-used for every polytope we want to integrate over. We then move our polytope $\mathbf{H} = \{\boldsymbol{x} \mid \mathbf{A}\boldsymbol{x} \leq \mathbf{b}\}$ from $\mathcal{H}$ description into its $\mathcal{V}$-description and call it $\mathbf{V}$ (L4, Algorithm 1). This operation has a complexity of $\mathcal{O}(m^{\lfloor n/2 \rfloor})$, with m being the number of inequalities [Chazelle, 1993], so polynomial for some fixed dimension n. Afterwards, we triangulate the vertices $\mathbf{V}$ into an array of simplices $\mathbf{S}$ (L6, Algorithm 1).

While finding the minimal triangulation is NP-complete [Kaibel and Pfetsch, 2002], finding some triangulation using the Delaunay-algorithm can be done in $\mathcal{O}(v^{\lceil n/2 \rceil})$ [Amenta et al., 2007], with v being the number of vertices obtained previously. These computations are also executed on the CPU using QHull [Barber et al., 1996]. We are now prepared for the actual numerical integration, which will happen on the GPU (L7, alg. 1).

This algorithm is detailed in Algorithm 2. It takes the polynomial q, points and weights $(\mathbf{R}, \mathbf{w})$ from the cubature rule and simplices $\mathbf{S}$. In practice, these are PyTorch [Paszke et al., 2019a] tensors. We then loop over each simplex in $\mathbf{s}_i$ (L2, Algorithm 2) and compute the cubature over all cubature points and weights $(\mathbf{R}, \mathbf{w})$ (L6, Algorithm 2). As these cubature points are distributed over the unit-simplex, we need a coordinate change to transform the points from the unit-simplex to points on $\mathbf{s}_i$ (L8, Algorithm 2), which is just a matrix-vector multiplication. We also need to calculate the absolute determinant of the Jacobian of this transformation for the pullback-measure, which coincides with the volume of the simplex (L5,Algorithm 2) and has the complexity n^3 due to the determinant. We then evaluate the polynomial on each point and add the sum weighted according to the cubature weight $\mathbf{w}$ (L10 and 13, Algorithm 2). In the end we sum up our integral over each simplex to arrive at the integral over our polytope (L15, Algorithm 2). In order to increase numerical accuracy, we first divide into positive and negative parts, sort each, and then sum up the elements via stableSum. In practice, this is done per batch in the inner loop, as it runs batched. Every loop in this algorithm, including over multiple monomials arising due to the symbolic integral, is done in parallel and leverages the parallelism of the GPU.

Finally, we want to stress that every computation in our algorithm uses established, heavily optimized numerical routines. This approach allows us to exploit the unique performance characteristics and heavy parallelism of GPUs to tackles this challenging problem. Therefore, the overall complexity of algorithm 2 is $\mathcal{O}(l_s \cdot (l_{gm} \cdot (n^2 + \log l_{gm}) + n^3) \log l_s)$, with l_s being the number of simplices and l_{gm} the number of cubature points.

This enables us to compute the overall complexity of gasp by noting that the number of simplices grows with $\mathcal{O}(m^{\lceil n/2 \rceil^2})$ [Seidel, 1995] with m being the number of inequalities. We arrive at $\mathcal{O}(m^{\lceil n/2 \rceil^2} \cdot (l_{gm} \cdot (n^2 + \log l_{gm}) + n^3) \lceil n/2 \rceil^2 \log m)$ and $l_{gm} = r \cdot \binom{r+n-1}{n-1}$. While this complexity seems unwieldy, we first want to note that the problem is fundamentally hard, as integrating an arbitrary polynomial over a single simplex is already NP-Hard [Baldoni et al., 2011]. Furthermore, in many applications, we can assume $dim(\mathbf{Y}) \ll dim(\mathbf{X})$ and therefore $dim(\mathbf{Y})$ is actually reasonable. Finally, we can amortize this computation as it must only be done once per constraint, enabling fast and efficient training.

C.2.2 Grundmann-Möller-Cubature

Algorithm 4 PrepareGrundmannMöller(d, n)

Input Total degree d, dimensions n
Output Cubature points $\mathbf{R} \in \mathbb{R}^{l_{gm} \times n}$ and weights $\mathbf{w} \in \mathbb{R}^{l_{gm}}$

$\mathbf{R} \leftarrow []$
$\mathbf{w} \leftarrow []$
$s \leftarrow \lceil \frac{d}{2} - 1 \rceil$
{According to Theorem 4 of Grundmann and Möller [1978]}
for $i \leftarrow 0$ **to** s **do**
  $w_i \leftarrow (-1)^i 2^{-2s} \frac{(d+n-2i)^d}{i!(d+n-i)!}$
  $\mathbf{\Gamma} \leftarrow$ combinationsSummingTo$(n, s-i)$
  {All combinations of n natural numbers summing to $s-i$}
  for $\boldsymbol{\gamma} \in \mathbf{\Gamma}$ **do**
    $\mathbf{r} \leftarrow \left(\frac{2\gamma_0+1}{d+n-2i}, \ldots, \frac{2\gamma_n+1}{d+n-2i} \right)$
    Append$(\mathbf{R}, \mathbf{r})$
    Append$(\mathbf{w}, w_i / \text{Len}(\Gamma))$
  end for
end for
return $\mathbf{R}, \mathbf{w}$

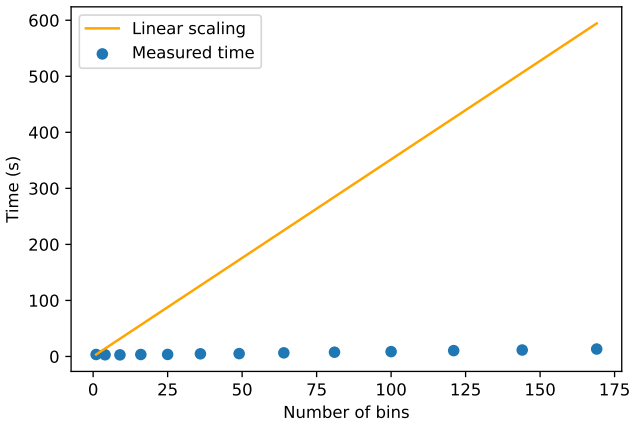

Figure 11: The integration time for splines on the Stanford drone dataset (scene 1) does not grow linearly with the number of bins. In this figure, we compare the time it takes to integrate our squared spline for an increasing number of bins versus a simple linear scaling, which we would expect if the empirical computational complexity per bin would stay approximately constant.

C.2.3 Overall Complexity

When analyzing the overall complexity of PAL, there are two major additional sources of computational complexity: the complexity of the SMT formula and, assuming the use of splines, the number of bins.

We will first focus on the complexity originating from the logical formula. The WMI problem in general is #P-hard [Zeng et al., 2020a]. Coarsely speaking, the SAE4WMI procedure may require exponential time in the worst case. It begins with an AllSMT step that enumerates all partial assignments satisfying the formula—potentially exponentially many. Each of these assignments is then checked for $\mathcal{LRA}$ consistency, which takes polynomial time per assignment. Afterwards, we have the integration of the polynomial on each polytope described by the $\mathcal{LRA}$-consistent truth assignment a task that is NP-hard in itself, as discussed in the previous section. Thus, the logical component alone can dominate the overall complexity, especially when the number of satisfying assignments grows rapidly. That said, this compilation cost is amortized: we pay it only once before training.

Another source of complexity arises from the number of bins when using a spline-based density, as our pipeline must be executed once per bin. While this might seem at first like a significant disadvantage for using a spline, in practice the complexity of the logical formula per bin, and therefore the overall time required for the compilation, decreases with an overall increasing number of bins. This is due to the space being partitioned into smaller and smaller patches as we increase the number of bins, with fewer constraints intersecting the average bin. For example, the time it takes to integrate a 169-bin spline over scene 1 of the Stanford drone dataset is just 3.77x the time it takes to integrate a spline with a single bin over the scene, instead of 169x. We show the relationship between linear scaling and our actual measured integration times in figure 11.

D ADDITIONAL RELATED WORKS

Other constraints in deep learning. Many approaches have been proposed for dealing with a variety of specialized constraints in neural networks. An abundant body of work investigates architectures that guarantee specific properties, such as monotonicity [You et al., 2017] or permutation invariance of inputs [Zaheer et al., 2017]. Other works impose constraints over they dynamics of a neural network, e.g., to follow a physics-based constraint or a PDE [Raissi et al., 2019, Li et al., 2020, Beltran et al., 2024]. These approaches are orthogonal to ours and cannot be easily generalized in our framework where constraints are algebraic.

Sampling with constraints. It is well known that (algebraic) constraints pose significant challenges for sampling procedures.Afshar et al. [2016] addressed these challenges with Markov Chain Monte Carlo, which is however unsuited for training PAL via gradient descent. Abboud et al. [2022] introduce an FPRAS scheme to approximate WMI problems whose constraints are represented in disjunctive normal form (DNF). While this approach provides some guarantees, it

would still require many samples to get an accurate estimate of a WMI integral and DNFs are not compact representations of many real-world constraints [Hoernle et al., 2022]. Another recent work on sampling under algebraic constraints is the Disjunctive Refinement Layer [Stoian and Giunchiglia, 2025], which is an iterative projection onto non-convex sets defined by quantifier-free conjunctions, disjunctions and negations of linear inequalities. It allows for sampling with guaranteed constraint satisfaction, but the iterative projection of the invalid probability mass leads to a clustering of projected samples at the boundaries and obstructs gradient flow.

Learning constraints. The problem of learning SMT($\mathcal{LRA}$) constraints from positive/negative examples was first addressed by INCAL [Kolb et al., 2018b], an incremental approach built upon SMT solvers. LARIAT [Morettin et al., 2020] addressed the problem of jointly learning the SMT($\mathcal{LRA}$) constraints and a piecewise polynomial density from unlabelled data. These two components are learned separately and then combined into a probabilistic model that can be queried using WMI solvers. In this paper, we assume the constraints are given and they are accounted for when learning the parameters of the density function. Combining `PAL` with the above approaches is an interesting future direction.

E EXPERIMENTAL DETAILS

E.1 REJECTION SAMPLING VS. `GASP!`

The polynomials with dimension n and total degree d we want to integrate are all of the form

$$\left(\sum_{\substack{\boldsymbol{\alpha}_i \in \mathbb{N}^n \\ 1^T \boldsymbol{\alpha}_i \leq d}} c_i \prod_j y_j^{\alpha_{ij}} \right)^2 .$$

The coefficients c_i are distributed as follows: $c_i \sum \pm\text{Poisson}(2)$, where $\pm$ denotes a random, equal chance, sign.

We generate the random simplices by following the same procedure as many times as needed:

1. draw a random unit simplex;
2. scale it between 0.5 and 1.5 (uniformly);
3. transform the vertices using a random orthonormal matrix;
4. translate it between 0 and 6;
5. keep the simplex if it does not overlap any previous simplex.

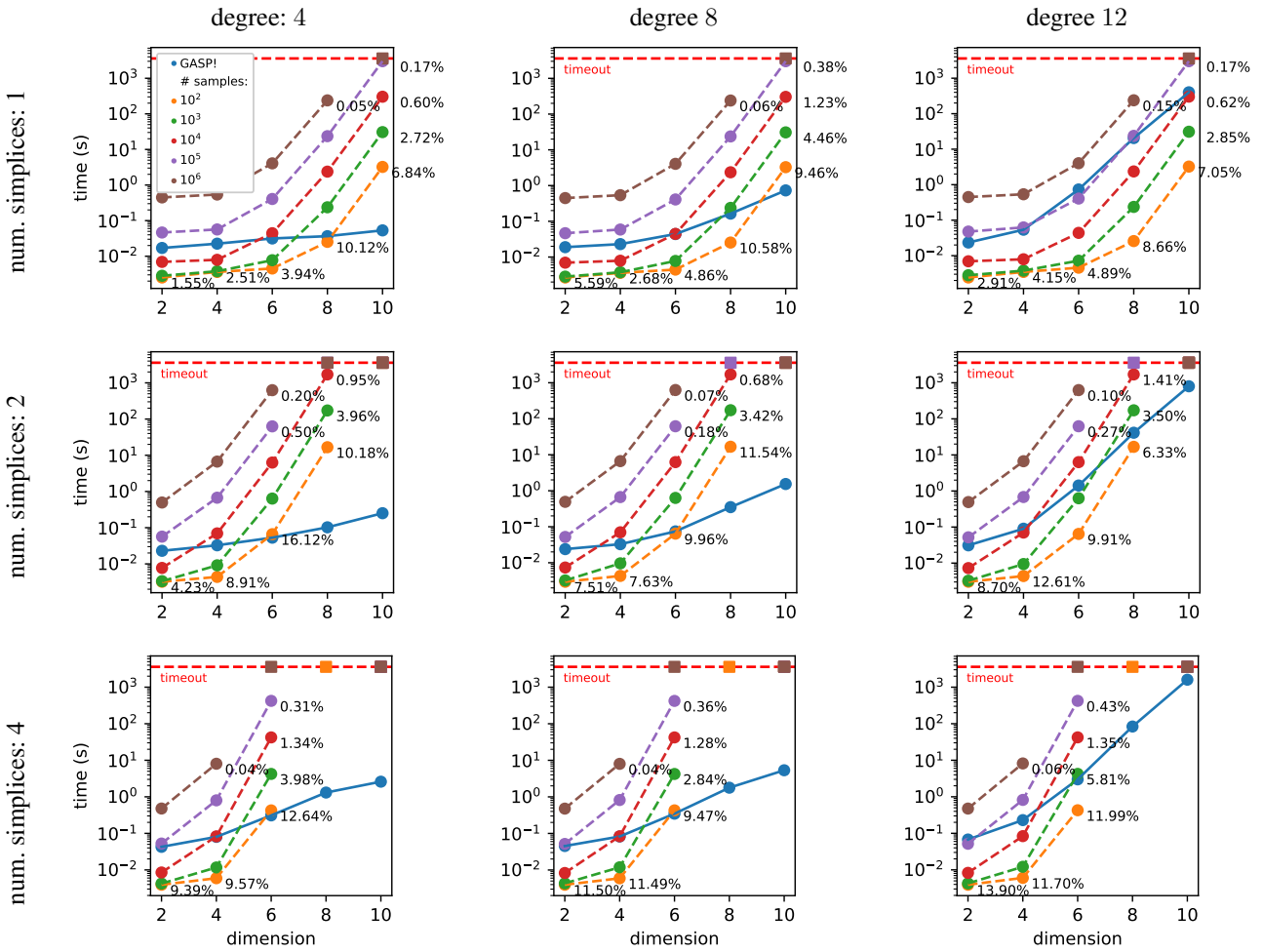

Figure 12: Runtime (in seconds) of rejection sampling vs a single GASP!-run for integrating random polynomials of varying degree over 4 random simplices. For rejection sampling, we additionally report its relative error. This benchmark was run using an NVIDIA RTX A6000, an AMD EPYC 7452 32-Core Processor and 528 Gigabyte RAM.

E.2 SAE4WMI(LATTE) VS. SAE4WMI(GASP!)

For this experiment, we used the benchmarking suite originally released with SAE4WMI [Spallitta et al., 2022] (https://github.com/unitn-sml/wmi-benchmarks) for generating random WMI problems. These instances are composed of a SMT($\mathcal{LRA}$) formula encoding the support of the distribution and a piecewise polynomial weight function. The weight functions have arbitrary SMT($\mathcal{LRA}$) conditions as internal nodes and non-negative polynomial leaves. In contrast with the benchmarks employed by Spallitta et al., our weight functions do not have sums or product as internal nodes. This minor modification was made to enforce a tighter control over the maximum overall degree of the weight function. The problems have $n \in \{3, 4, 5\}$ real variables and are generated in a recursive manner, with formulas and weight functions having depth $r \in \{2, 3, 4\}$, the latter having polynomial leaves with maximum degree $d \in \{0, 2, 4\}$. For each configuration of $\langle n, d, r \rangle$, we generated 10 instances, for a total of 270 WMI problems. This benchmark was run using an NVIDIA RTX A6000, an AMD EPYC 7452 32-Core Processor and 528 Gigabyte RAM.

E.2.1 GASP! vs SymPy

Another option is to compare the whole GASP! pipeline, including PA [Morettin et al., 2017] to enumerate the convex Polytopes, to a completely orthogonal approach. XADD [Kolb et al., 2018a] tackles the weighted model integral via symbolic manipulations. In practice, this means integrating via an explicit anti-derivative and then replacing the variable

with the symbolic lower and upper bounds, analogously on how solving an integral by hand is done. As the symbolic polynomial is represented using SymPy [Meurer et al., 2017b], our polynomial over both variables and coefficients can be naturally expressed and running XADD [Kolb et al., 2018a] on this polynomial directly results in $I_\phi(\mathbf{\Lambda})$. We benchmark GASP! vs. XADD equipped with SymPy on the NStar-constraints, which is just an n-pointed star where we always connect with opposite points. An example of the constraints can be seen in figure 9. Using our algorithm GASP!, we were able to reduce the runtime for the integral a polynomial of total degree 12 for a star with 17 corners from 6 hours and 20 minutes to 19 seconds, a significant speedup of 3 magnitudes or approximately 1200 times faster. Detailed results for the benchmark are in the Appendix in table 4 and 5.

total degree n	0	1	4	6	8	10	12
3	00:00:00	00:00:00	00:00:00	00:00:02	00:00:05	00:00:17	00:00:40
5	00:00:01	00:00:01	00:00:05	00:00:14	00:00:41	00:02:09	00:05:19
7	00:00:04	00:00:06	00:00:14	00:00:42	00:02:04	00:07:07	00:17:55
9	00:00:10	00:00:14	00:00:33	00:01:43	00:05:14	00:19:19	00:49:46
11	00:00:19	00:00:25	00:01:01	00:03:14	00:10:02	00:37:02	01:36:09
13	00:00:31	00:00:41	00:01:38	00:05:08	00:15:51	00:59:36	02:36:15
15	00:00:53	00:01:09	00:02:42	00:08:21	00:25:55	01:37:29	04:19:17
17	00:01:17	00:01:39	00:03:46	00:11:28	00:35:24	02:16:39	06:20:02

Table 4: We show the results for integrating the NSTar-Benchmark using the XADD-Algorithm equipped with SymPy [Kolb et al., 2018a]. Results in $hh : mm : ss$.. This benchmark was run on the same machine as in 5. This benchmark was run using an NVIDIA RTX A6000, an AMD EPYC 7452 32-Core Processor and 528 Gigabyte RAM. The results for GASP! are provided in table 5.

total degree n	0	1	4	6	8	10	12
3	00:00:00	00:00:00	00:00:00	00:00:00	00:00:01	00:00:04	00:00:10
5	00:00:00	00:00:00	00:00:00	00:00:00	00:00:01	00:00:06	00:00:15
7	00:00:00	00:00:00	00:00:00	00:00:00	00:00:01	00:00:06	00:00:16
7	00:00:00	00:00:00	00:00:00	00:00:00	00:00:01	00:00:06	00:00:16
9	00:00:00	00:00:00	00:00:00	00:00:01	00:00:02	00:00:07	00:00:16
11	00:00:01	00:00:01	00:00:01	00:00:01	00:00:02	00:00:07	00:00:16
13	00:00:02	00:00:02	00:00:02	00:00:02	00:00:03	00:00:08	00:00:17
15	00:00:02	00:00:02	00:00:02	00:00:03	00:00:04	00:00:09	00:00:18
17	00:00:03	00:00:03	00:00:03	00:00:04	00:00:05	00:00:10	00:00:19

Table 5: GASP! is significantly faster compared to XADD [Kolb et al., 2018a]. We show results for integrating the NSTar-Benchmark using GASP!. Results in $hh : mm : ss$.. This benchmark was run using an NVIDIA RTX A6000, an AMD EPYC 7452 32-Core Processor and 528 Gigabyte RAM. The results for XADD are provided in table 4.

E.3 NSTAR

For the NStar dataset, we generate 800.000 $(\boldsymbol{x}, \boldsymbol{y})$-points on the NStar via rejection sampling. The NStar-constraints are formed by taking the n-pointed star on the circle with radius 10, where the the constraints are constructed by connecting each corner-point with the two most-opposite points. The distribution of $\mathbf{X}$ is uniform over the star, the distribution of $\mathbf{Y}$ is a cauchy-distribution with location $\mathbf{X}$ and scale $1.5\sqrt{10}$. The star is located in $[-10, 10]^2$.

We form train, test and validation datasets by dividing the points with a share of 70%, 15% and 15%.

E.3.1 Models

All models are trained with a batch-size of 512.

PAL We will now describe our settings for the PAL-models on the NStar-Dataset. For every variant of the star, we perform a grid-search over the following configurations, picking the best-performing according to the log-likelihood on the held-out dataset:

- epochs: 1500
- learning rate:$1e-06$, $1e-05$
- network hidden layers: $[1024, 1024]$, $[1024]$

The network is a fully-connected neural network using ReLU [Glorot et al., 2011] as activations. We use the schedule-free version of Adam [Defazio et al., 2024]. We use a single polynomials, with the re-parametrization as detailed in Appendix B.1 and train using a loss composed of log-likelihood and a penalty on very large integral-values detailed in Appendix B.3.

In this experiment, our density is modeled by a single, squared polynomial over $\mathbf{Y}$ with the maximum number of terms given the required total degree. So, for example, the polynomial with a total degree of 10 squared has a total degree of 5 unsquared. Therefore we collect all multivariate monomials up to the total degree of 5 to build our parametrized polynomial over $\mathbf{Y}$.

GMM For the GMM-Models, we perform the following grid-search:

- covariance: full and independent (although full covariance leads to better performing models for our dataset)
- epochs: 1500
- learning rate: $1e-04$, $1e-05$
- network hidden layers: $[1024, 1024]$, $[1024]$

We use the Adam optimizer [Kingma and Ba, 2015a].

DSP For DeepSeaProbLog, when performing the grid-search, we select the model according to the loss with the constant, final multiplier for the continous approximation for the inequality. The grid is over the following parameters:

- epoch: 1500
- learning rate: 0.001, 0.0001, 0.00001
- minimum-multiplier for the inequality-relaxation: 0.1, 1.0
- maximum-multiplier: 5
- network hidden layers: $[1024, 1024]$, $[1024]$
- optimiser: AdaMax and Adam [Kingma and Ba, 2015a]

Due to the slower training speed, we train DSP with a patience of 200-epochs (the other models are picked as the model with the best validation-score over all 1500 epochs). Finally, we train with sampling 50 times per input $\boldsymbol{x}^{(b)}$ in order to approximate $P(valid)$.

DSP is trained by optimizing both the fit on the data, as well as constraint satisfaction:

$$l_{dsp}(\boldsymbol{x}^{[1:b]}, \boldsymbol{y}^{[1:b]}) = \sum_i (-1) \cdot \log p(\boldsymbol{y}^i | \boldsymbol{x}^i) + \mathsf{CE}(p(\mathbf{Y} \models \phi \mid \mathbf{X} = \boldsymbol{x}^i)) \tag{DSP-Loss}$$

where $p(\mathbf{Y} \models \phi \mid \mathbf{X} = \boldsymbol{x}^i)$ is approximated numerically in DSP in comparison to PAL. CE denotes the binary cross-entropy loss against the constant 1 label.

E.3.2 Results

	NN + PAL			NN + GMM				DeepSeaProblog	
N	deg 10	deg 14	deg 18	K=1	K=4	K=8	K=32	by LL	by Loss
3	-4.749 ±0.169	**-4.674 ±0.009**	-4.840 ±0.251	-5.016 ±0.001	-4.792 ±0.003	-4.740 ±0.003	-4.723 ±0.006	-5.027 ±0.012	-42.821 ±41.989
7	-4.529 ±0.008	**-4.527 ±0.009**	-4.741 ±0.287	-5.009 ±0.000	-4.850 ±0.014	-4.708 ±0.007	-4.612 ±0.005	-5.019 ±0.010	-206.411 ±132.409
11	**-4.570 ±0.223**	-4.584 ±0.171	-4.591 ±0.180	-4.988 ±0.000	-4.922 ±0.015	-4.791 ±0.018	-4.620 ±0.008	-83.042 ±58.990	-43.151 ±42.199
19	-4.506 ±0.034	**-4.492 ±0.004**	4.616 ±0.228	-4.995 ±0.000	-4.981 ±0.003	-4.925 ±0.010	-4.652 ±0.003	-5.001 ±0.001	-155.139 ±101.533

Table 6: Average log-likelihood on the test-set for the NStar-dataset. We test on a 3, 7, 11 and 19-Star and compare our approach (NN+PAL) to a conditional GMM and the neural distributional fact fitted by DeepSeaProblog. For DeepSeaProblog, we report the performance of two model, one selected by best log-likelihood (LL) and one by best loss (Loss), which takes into consideration both the fit and the probability of violating the constraints. After choosing the hyper-parameters, all runs were repeated 10-times and we report mean and standard deviation.

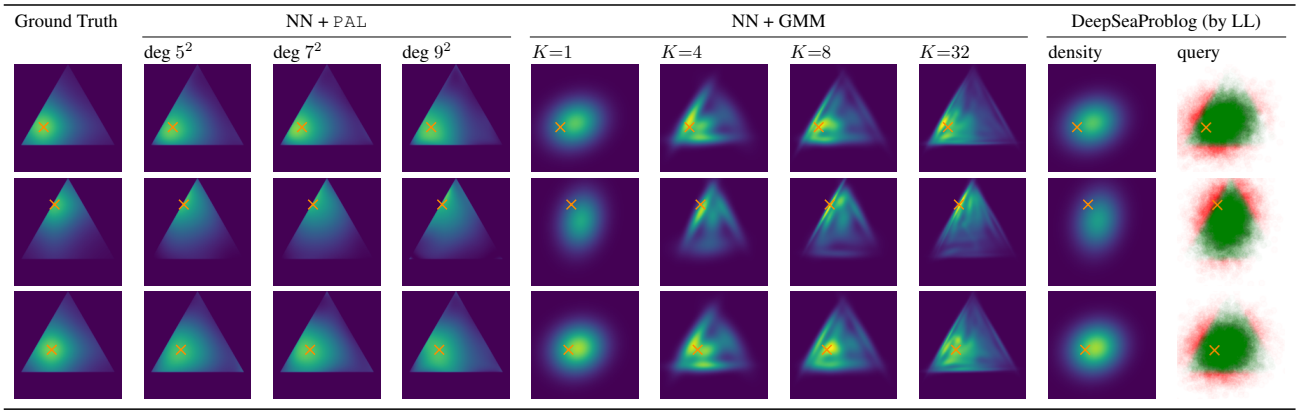

Table 7: Densities of the Ground-Truth compared to the polynomial, GMM and DeepSeaProbLog for the 3-Star problem with a cauchy-density. For the DSP model selected by log-likelihood, we show the density of the neural distributional fact, and we also show the result of querying the ProbLog program representing our constraints 10000 times. The samples associated with an true-label are shown in green, the samples associated with a false-label are shown in red.

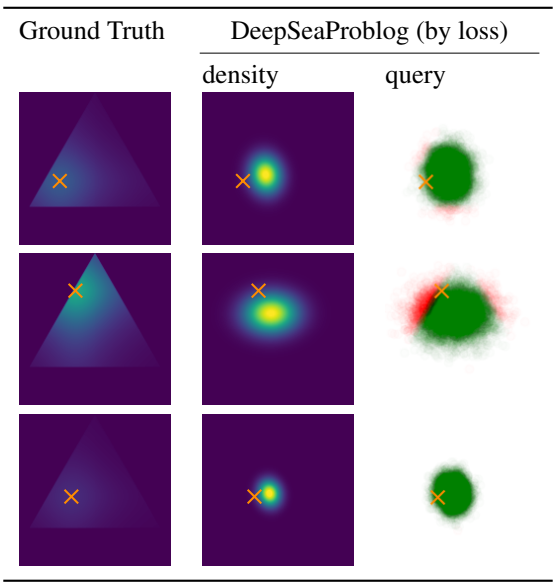

Table 8: Densities of the Ground-Truth compared to the DeepSeaProbLog for the 3Star problem with a cauchy-density. DeepSeaProbLog is selected by loss, and due to avoiding the constraints, more concentrated and therefore visualized separately. We show the density for the neural distributional fact and the samples obtained by the query. The samples associated with an true-label are shown in green, the samples associated with a false-label are shown in red. We choose to visualize this separately in order to keep the color-scheme in figure 7 reasonable.

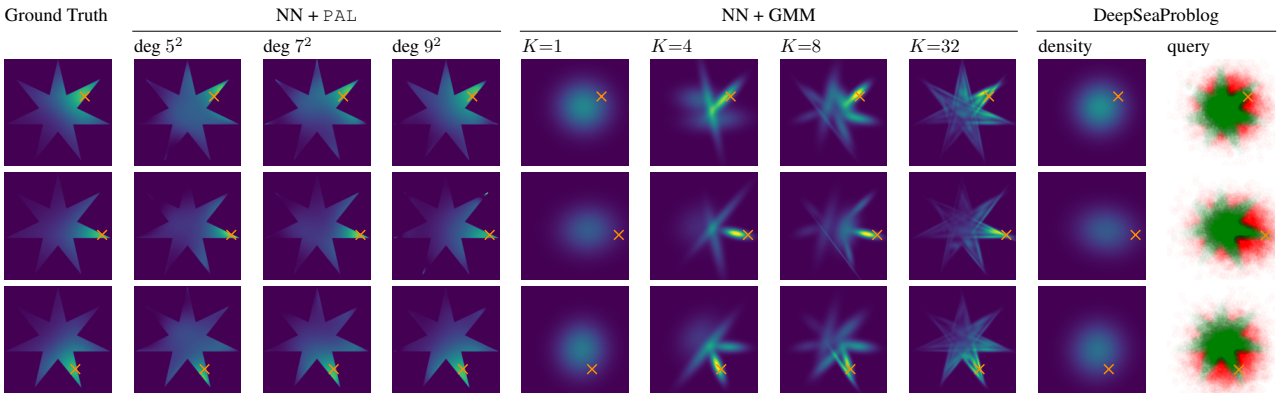

Table 9: Densities of the Ground-Truth compared to the polynomial, GMM and DeepSeaProbLog for the 7-Star problem with a cauchy-density. For the DSP model selected by log-likelihood, we show the density of the neural distributional fact, and we also show the result of querying the ProbLog program representing our constraints 10000 times. The samples associated with an true-label are shown in green, the samples associated with a false-label are shown in red.

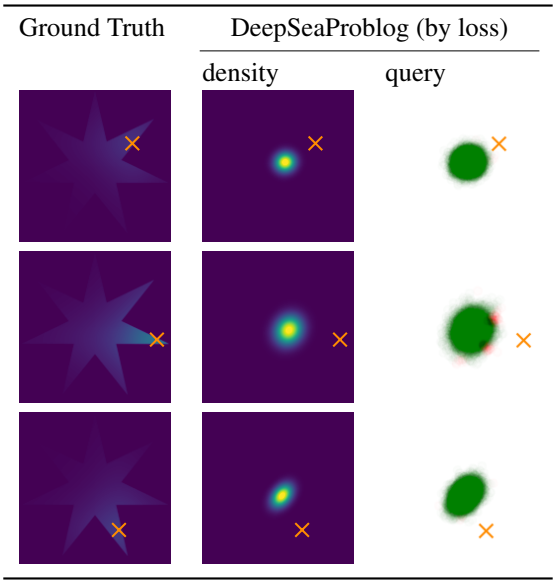

Table 10: Densities of the Ground-Truth compared to the DeepSeaProbLog for the 7Star problem with a cauchy-density. DeepSeaProbLog is selected by loss, and due to avoiding the constraints, more concentrated and therefore visualized separately. We show the density for the neural distributional fact and the samples obtained by the query. The samples associated with an true-label are shown in green, the samples associated with a false-label are shown in red. We choose to visualize this separately in order to keep the color-scheme in figure 9 reasonable.

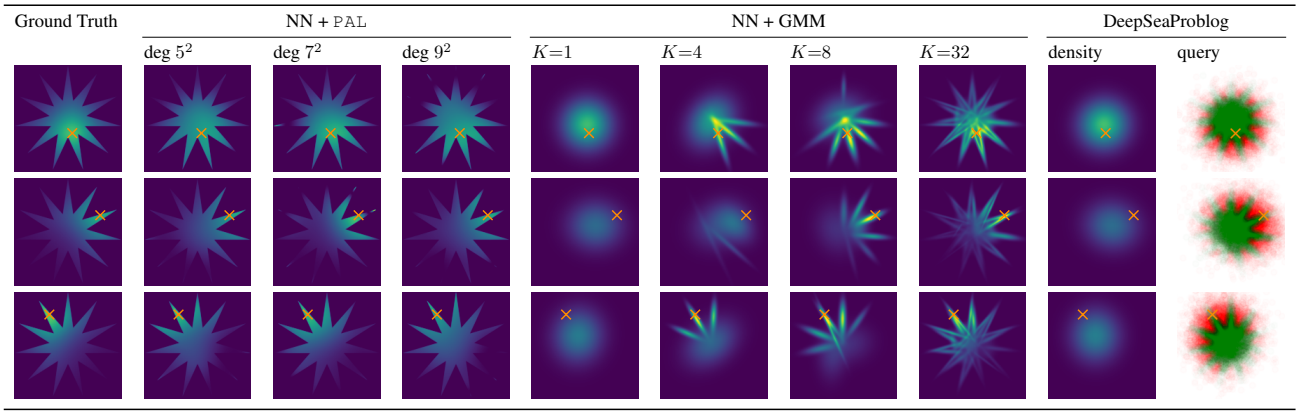

Table 11: Densities of the Ground-Truth compared to the polynomial, GMM and DeepSeaProbLog for the 11-Star problem with a cauchy-density. For the DSP model selected by log-likelihood, we show the density of the neural distributional fact, and we also show the result of querying the ProbLog program representing our constraints 10000 times. The samples associated with an true-label are shown in green, the samples associated with a false-label are shown in red.

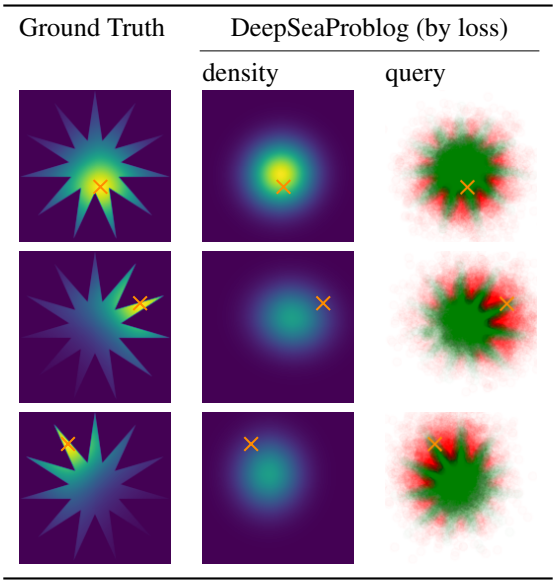

Table 12: Densities of the Ground-Truth compared to the DeepSeaProbLog for the 11Star problem with a cauchy-density. DeepSeaProbLog is selected by loss, and due to avoiding the constraints, more concentrated and therefore visualized separately. We show the density for the neural distributional fact and the samples obtained by the query. The samples associated with an true-label are shown in green, the samples associated with a false-label are shown in red. We choose to visualize this separately in order to keep the color-scheme in figure 11 reasonable.

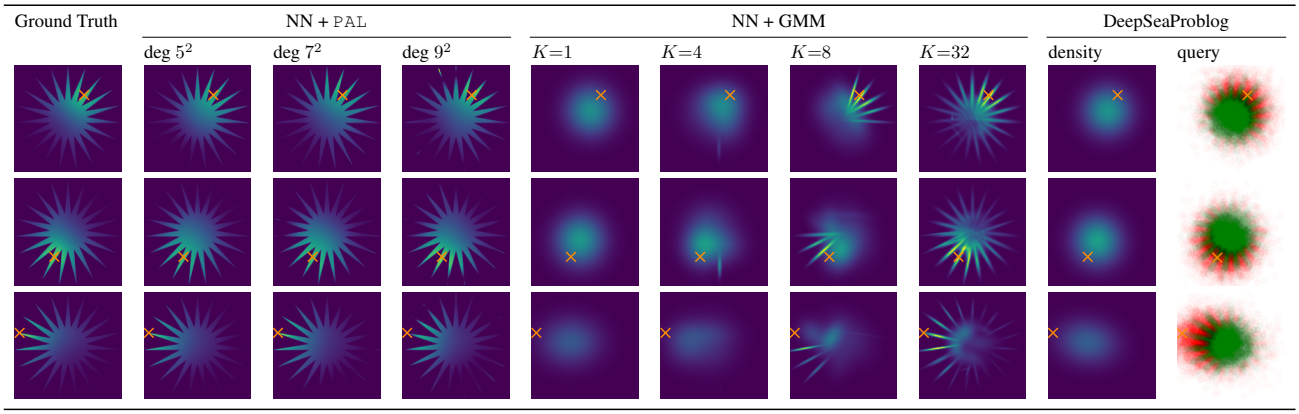

Table 13: Densities of the Ground-Truth compared to the polynomial, GMM and DeepSeaProbLog for the 19-Star problem with a cauchy-density. For the DSP model selected by log-likelihood, we show the density of the neural distributional fact, and we also show the result of querying the ProbLog program representing our constraints 10000 times. The samples associated with a true-label are shown in green, the samples associated with a false-label are shown in red.

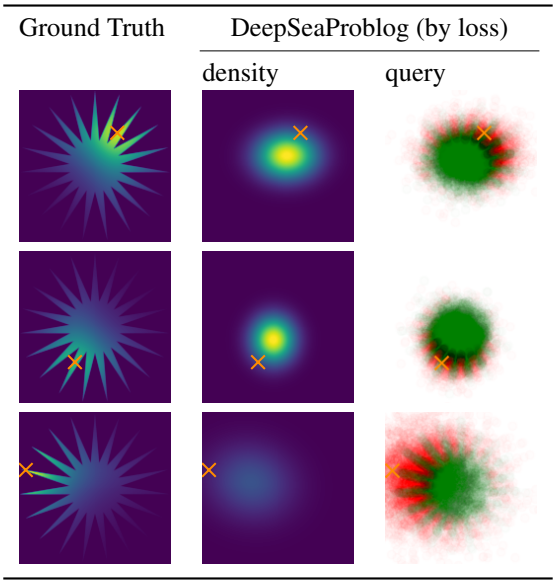

Table 14: Densities of the Ground-Truth compared to the DeepSeaProbLog for the 19Star problem with a cauchy-density. DeepSeaProbLog is selected by loss, and due to avoiding the constraints, more concentrated and therefore visualized separately. We show the density for the neural distributional fact and the samples obtained by the query. The samples associated with an true-label are shown in green, the samples associated with a false-label are shown in red. We choose to visualize this separately in order to keep the color-scheme in figure 13 reasonable.

E.4 STANFORD DRONE DATASET - JOINT DISTRIBUTION

E.4.1 Details of the Dataset - Scenario 1

We focus on image 12, the image with the most trajectories. We first want to note that the time-resolution, due to it being extracted from a 30-fps video, is quite high. In order to eliminate outliers, we first delete all points without movement (trajectories with a total variance of less than 20 and points with a distance of less than 0.1 compared to the previous). Then, we clean the data by discarding all short trajectories (= length of less than 50). We arrive at 415 moving trajectories out of the 499 we started with. We split this dataset, by trajectory, into train, test and validation (70%, 15% and 15%) and then concatenate all the points. We arrive at 124998 train points, 26786 validation points and 26786 test points. While this appears like a significant of points, we want to stress that many are heavily autocorrelated due to the high resolution, and the actual, total, amount of trajectories is only 415.

type	detail	num. params	$\Pr(\neg\phi)$	log-like
PAL (Spline)	8 knots, 10 mixtures	330	**0.000**	-3.013 ±0.002
PAL (Spline)	8 knots, 8 mixtures	264	**0.000**	3.023 ±0.003
PAL (Spline)	8 knots, 4 mixtures	132	**0.000**	-3.067 ±0.009
PAL (Spline)	10 knots, 10 mixtures	410	**0.000**	-2.984 ±0.002
PAL (Spline)	10 knots, 8 mixtures	328	**0.000**	-2.995 ±0.005
PAL (Spline)	10 knots, 4 mixtures	164	**0.000**	-3.045 ±0.008
PAL (Spline)	12 knots, 10 mixtures	490	**0.000**	-2.971 ±0.003
PAL (Spline)	12 knots, 8 mixtures	392	**0.000**	-2.979 ±0.003
PAL (Spline)	12 knots, 4 mixtures	196	**0.000**	-3.025 ±0.010
PAL (Spline)	14 knots, 10 mixtures	570	**0.000**	-2.950 ±0.002
PAL (Spline)	14 knots, 8 mixtures	456	**0.000**	-2.961 ±0.002
PAL (Spline)	14 knots, 4 mixtures	228	**0.000**	-3.009 ±0.008
PAL (Spline)	16 knots, 10 mixtures	650	**0.000**	-2.937 ±0.003
PAL (Spline)	16 knots, 8 mixtures	520	**0.000**	-2.948 ±0.003
PAL (Spline)	16 knots, 4 mixtures	260	**0.000**	-2.998 ±0.010
GMM	K=5	30	≈ 12.475 ±0.761	-3.359 ±0.034
GMM	K=10	60	≈ 8.887 ±0.224	-3.223 ±0.008
GMM	K=20	120	≈ 4.229 ±0.142	-3.081 ±0.012
GMM	K=50	300	≈ 2.375 ±0.112	-2.983 ±0.004
GMM	K=100	600	≈ 1.190 ±0.052	**-2.917 ±0.005**
Flow	1 transformation (t), 128x2 hidden	22830	≈ 5.643 ±0.487	-3.098 ±0.013
Flow	1 transformation (t), 64x2 hidden	7342	≈ 5.245 ±0.516	-3.089 ±0.017
Flow	1 transformation (t), 32x2 hidden	2670	≈ 5.651 ±0.596	-3.109 ±0.016
Flow	2 transformations (t), 128x2 hidden	45660	≈ 2.616 ±0.221	-2.986 ±0.008
Flow	2 transformations (t), 64x2 hidden	14684	≈ 2.157 ±0.250	-2.972 ±0.011
Flow	2 transformations (t), 32x2 hidden	5340	≈ 2.468 ±0.612	-2.979 ±0.016
Flow	5 transformations (t), 128x2 hidden	114150	≈ 1.771 ±0.159	-2.940 ±0.007
Flow	5 transformations (t), 64x2 hidden	36710	≈ 1.930 ±0.130	-2.949 ±0.007
Flow	5 transformations (t), 32x2 hidden	13350	≈ 1.677 ±0.231	-2.943 ±0.012
Flow	10 transformations (t), 128x2 hidden	228300	≈ 1.502 ±0.109	-2.919 ±0.007
Flow	10 transformations (t), 64x2 hidden	73420	≈ 1.698 ±0.202	-2.943 ±0.018
Flow	10 transformations (t), 32x2 hidden	26700	≈ 1.826 ±0.252	-2.938 ±0.007

Table 15: Results for the $p(\mathbf{Y})$-case of the Stanford-Drone dataset for scenario 1. All Spline models have equal number of knots in y_1 and y_2. The average percent of probability mass covering invalid space ($\Pr(\neg\phi)$) over our test-set is given in percent. After choosing the hyper-parameters, all runs were repeated 10-times and we report mean and standard deviation.

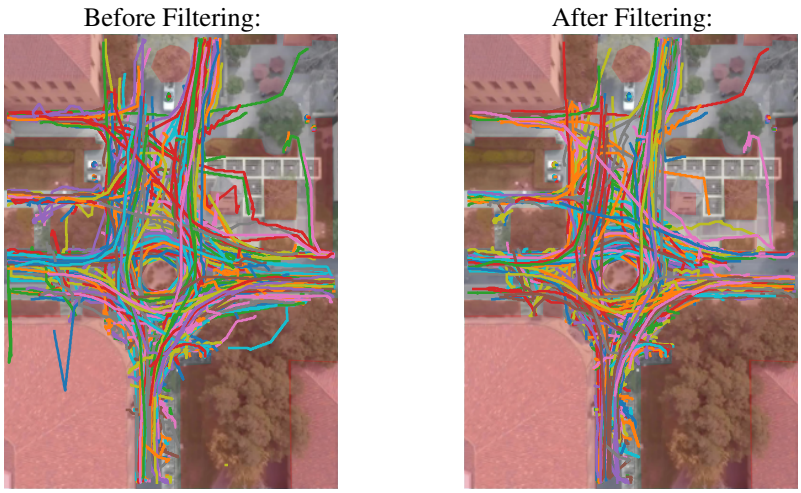

Figure 13: The trajectories before/after filtering for image 12 in the Stanford Drone Dataset. The constraints are shown in red.

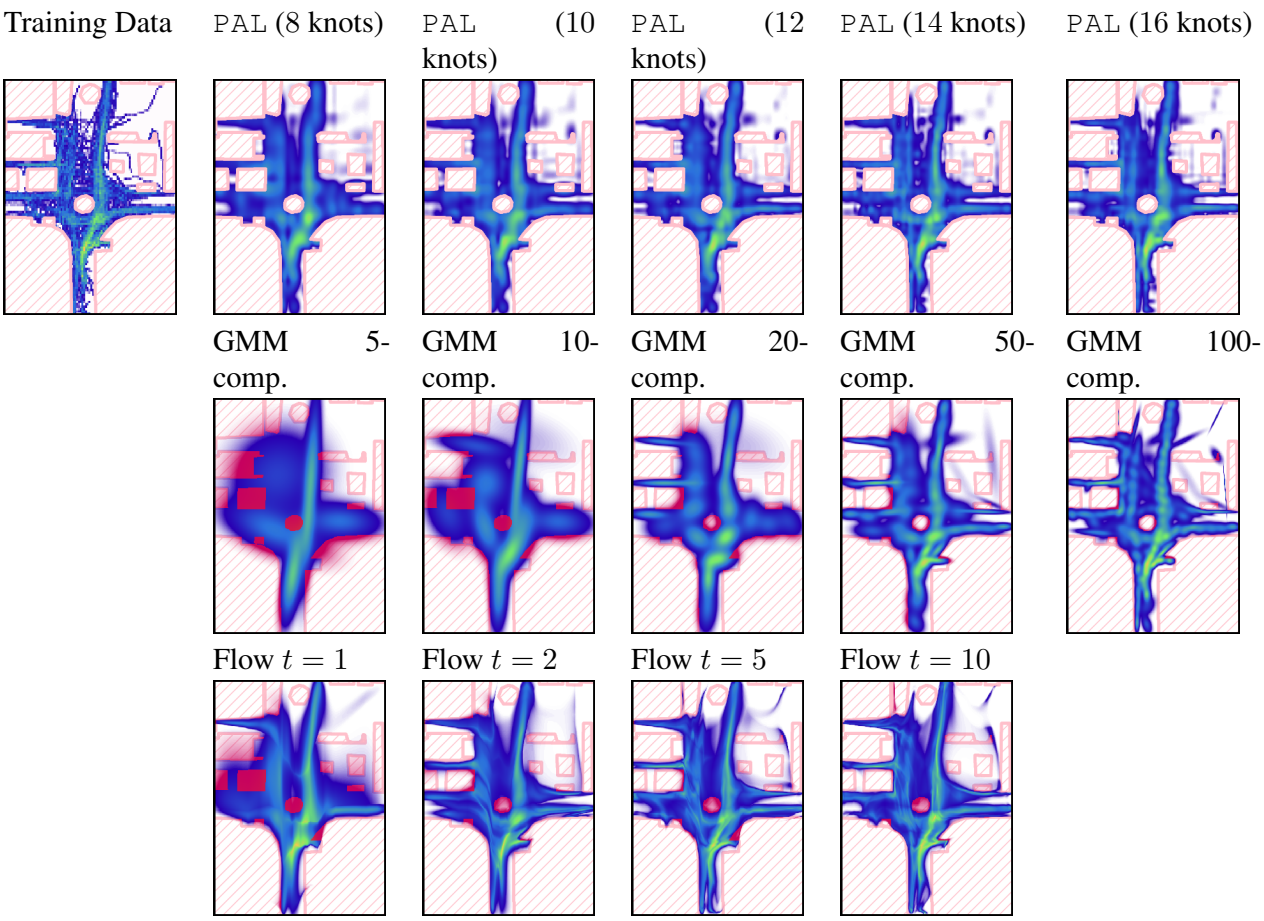

Table 16: Densities on the $p(\mathbf{Y})$-case of the Stanford-Drone dataset for scenario 1. All Spline models have 10-mixture components and equal number of knots in Y_1 and Y_2. The flow-models have two hidden layers of size 128 per transformation.

E.4.2 Details of the Dataset - Scenario 2

We focus on image 2, which consists only of 119 trajectories. We perform the same filtering etc. as in scenario 1 and arrive at 53504 train points, 10197 validation points and 13860 test points.

type	detail	num. params	perc. invalid	log-like
PAL (Spline)	8 knots, 10 mixtures	330	**0.000**	-3.376 ±0.007
PAL (Spline)	8 knots, 8 mixtures	264	**0.000**	-3.376 ±0.007
PAL (Spline)	10 knots, 10 mixtures	410	**0.000**	-3.348 ±0.005
PAL (Spline)	10 knots, 8 mixtures	328	**0.000**	-3.362 ±0.006
PAL (Spline)	12 knots, 10 mixtures	490	**0.000**	-3.329 ±0.003
PAL (Spline)	12 knots, 8 mixtures	392	**0.000**	-3.343 ±0.004
PAL (Spline)	14 knots, 10 mixtures	570	**0.000**	-3.313 ±0.003
PAL (Spline)	14 knots, 8 mixtures	456	**0.000**	-3.333 ±0.007
PAL (Spline)	16 knots, 10 mixtures	650	**0.000**	-3.301 ±0.004
PAL (Spline)	16 knots, 8 mixtures	520	**0.000**	-3.322 ±0.004
GMM	K=5	35	≈ 12.220 ±0.053	-3.701 ±0.002
GMM	K=10	70	≈ 6.589 ±0.283	-3.564 ±0.012
GMM	K=20	140	≈3.223 ±0.542	-3.449 ±0.019
GMM	K=50	350	≈ 1.289 ±0.159	-3.351 ±0.014
GMM	K=100	700	≈ 0.656 ±0.042	**-3.259 ±0.005**
Flow	1 transformation (t), 32x2 hidden	2670	≈ 2.274 ±0.214	-3.431 ±0.012
Flow	2 transformations (t), 32x2 hidden	5340	≈ 1.210 ±0.285	-3.332 ±0.020
Flow	5 transformations (t), 32x2 hidden	13350	≈ 0.710 ±0.126	-3.266 ±0.015
Flow	10 transformations (t), 32x2 hidden	26700	≈ 0.867 ±0.126	-3.273 ±0.012

Table 17: Results for the $p(\mathbf{Y})$-case of the Stanford-Drone dataset for scenario 2. All Spline models have equal number of knots in y_1 and y_2. The average percent of probability mass covering invalid space ($\Pr(\neg\phi)$) over our test-set is given in percent. After choosing the hyper-parameters, all runs were repeated 10-times and we report mean and standard deviation.

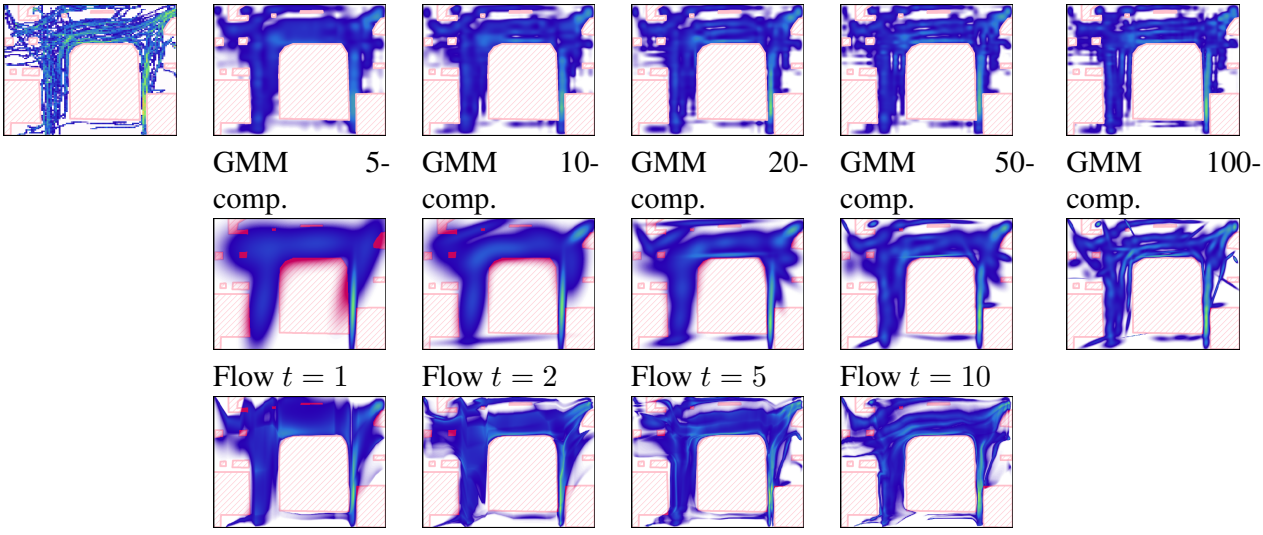

Table 18: Densities on the $p(\mathbf{Y})$-case of the Stanford-Drone dataset for scenario 2. All Spline models have 10-mixture components and equal number of knots in Y_1 and Y_2. The flow-models have two hidden layers of size $32x2$ per transformation.

E.5 STANFORD DRONE DATASET - CONDITIONAL DISTRIBUTIONS

E.5.1 Details of the Dataset

The goal in this task is to fit the distribution of possible future trajectories, so if our random variable for the coordinates at timestep t is $\mathbf{C}_t$, then our goal is to predict $\mathbf{Y} = \mathbf{C}_{t \geq t'}$ given the current a window of 5 equidistant points $\mathbf{X} = (\mathbf{C}_{t=t'-0\cdot\Delta}, \mathbf{C}_{t=t'-1\cdot\Delta}, \ldots, \mathbf{C}_{t=t'-5\cdot\Delta})$, with Δ being some step-size. This challenging construction induces multi-modality and uncertainty in the predictive distribution, because if there is a chance of visiting a certain area in the future given the 5 steps, it must have some probability mass assigned to it.

In order to bias our models towards more well-connected paths, we bias the network towards the closer in time datapoints. The distribution is therefore a mixture of both a uniform distribution over the whole future trajectory and a uniform distribution over the future trajectory of length step-size s, so 70 in our case. Both choices have equal chance.

E.5.2 Scenario 1

For this task, we focus on image 12, the image with the most trajectories. We want to note that the time-resolution, due to it being extracted from a 30-fps video, is quite high. As we want to focus on the trajectory, we eliminate all points without movement, so points with a distance of less than 0.1 compared to the previous. We take a step-size of 70 for the window of 5 points that form our $\mathbf{X}$, which we will slide through the trajectory. We also discard all trajectories that are too short to fill our window, so where the length is less than $5 \cdot 70$, as we want to focus on long trajectories. We split the trajectories into 70% train, 15% validation and 15% test. We then create a static validation and test-dataset by sampling 10 future $\mathbf{Y}$ points per window $\mathbf{X} = \boldsymbol{x}$ at creation statically. For the train-dataset, we sample the during training, so for the same $\mathbf{X} = \boldsymbol{x}$ it will see different future points. We arrive at 22619-train datapoints, with $\mathbf{Y}$ dynamically sampled per $\mathbf{X} = \boldsymbol{x}$, 42740-validation datapoints and 49660-test datapoints.

Model Details

All our models are simple, fully connected neural networks with ReLu as an activation function [Glorot et al., 2011].

We denote the following sizes:

- **large**: 2 hidden layers of size 2048 each
- **medium**: 2 hidden layers of size 1024 each
- **small**: 2 hidden layers of size 512 each

We train all models for a maximum of 500 epochs with a patience of 20 epochs and run the hyper-parameter search for each network-size per model-type.

`PAL` For the `PAL` models, we do a grid-search over the following parameters:

- **number of mixtures**: 8 and 10
- **number of knots**: 10 and 14 (equal over y_1 and y_2)
- **optimizer** AdamW schedulefree [Defazio et al., 2024] with learning rate: 0.001, 0.0001, 0.00001 and batch-sizes 16, 32 and 128
- **net-sizes**: large/medium/small

GMM For the conditional GMM-models, we do a grid-search over the following parameters:

- **number of components** K: 4, 32, 50, 80, 100 with full covariances
- **net-sizes**: large/medium/small
- **optimizer** Adam [Kingma and Ba, 2015b] with learning rates: 0.001, 0.0001, 0.00001 and batch-sizes 16, 32 (128 led to worse performance due to overfitting on initial-runs and was excluded)

DSP For the DSP models, we do a grid-search over the following parameters:

- **optimizer** AdaMax [Kingma and Ba, 2015b] with learning rates 0.01, 0.001, 0.0001, 0.00001 and batch-sizes 16, 32 (128 led to worse performance due to overfitting on initial-runs and was excluded)
- **annealing starting-multiplier**: 0.1, 1.0
- **end-multiplier**: 5
- **net-sizes**: large/medium/small

We use a tanh-scaling of the annealing multiplier with an alpha of $1e-4$ and train with the loss DSP-Loss.

Results

type	size dist.	net size	log-like	num. params dist.	$\mathsf{Pr}(\neg\phi)$
PAL (Spline)	14 knots, 10 mixtures	medium	-2.209 $\pm$0.136	570	**0.000**
PAL (Spline)	10 knots, 8 mixtures	medium	-2.942 $\pm$1.204	328	**0.000**
PAL (Spline)	14 knots, 8 mixtures	small	**-2.086 $\pm$0.144**	456	**0.000**
PAL (Spline)	10 knots, 8 mixtures	small	-2.272 $\pm$0.130	328	**0.000**
PAL (Spline)	14 knots, 10 mixtures	large	-2.174 $\pm$0.120	570	**0.000**
PAL (Spline)	10 knots, 8 mixtures	large	-2.263 $\pm$0.168	328	**0.000**
GMM	K=100	medium	-3.323 $\pm$0.738	700	$\approx$ 20.191 $\pm$1.937
GMM	K=80	medium	-11.173 $\pm$8.202	560	$\approx$ 72.969 $\pm$34.192
GMM	K=50	medium	-2.932 $\pm$0.361	350	$\approx$ 21.706 $\pm$2.727
GMM	K=32	medium	-2.989 $\pm$0.345	224	$\approx$ 21.620 $\pm$2.672
GMM	K=4	medium	-3.262 $\pm$0.379	28	$\approx$ 20.955 $\pm$1.366
GMM	K=100	small	-2.838 $\pm$0.485	700	$\approx$ 20.321 $\pm$1.672
GMM	K=80	small	-2.835 $\pm$0.410	560	$\approx$ 20.096 $\pm$1.964
GMM	K=50	small	-2.644 $\pm$0.258	350	$\approx$ 20.989 $\pm$1.774
GMM	K=32	small	-2.735 $\pm$0.379	224	$\approx$ 19.842 $\pm$1.584
GMM	K=4	small	-3.235 $\pm$0.970	28	$\approx$ 21.859 $\pm$1.600
GMM	K=50	large	-3.074 $\pm$0.273	350	$\approx$ 24.721 $\pm$3.632
GMM	K=32	large	-6.383 $\pm$6.179	224	$\approx$ 36.660 $\pm$33.943
GMM	K=100	large	-4.963 $\pm$4.690	700	$\approx$ 30.516 $\pm$24.794
GMM	K=80	large	-16.420 $\pm$9.413	560	$\approx$ 83.409 $\pm$31.042
GMM	K=4	large	-7.553 $\pm$5.529	28	$\approx$ 48.345 $\pm$35.762
DSP (by loss)	1 Gaussian	large	-8.532 $\pm$11.325	6	$\approx$ 29.035 $\pm$3.074
DSP (by loss)	1 Gaussian	medium	-6.176 $\pm$5.132	6	$\approx$ 36.648 $\pm$9.670
DSP (by loss)	1 Gaussian	small	-3.876 $\pm$0.466	6	$\approx$ 49.046 $\pm$16.395
DSP (by log-like)	1 Gaussian	large	-8.520 $\pm$11.330	6	$\approx$ 34.963 $\pm$9.933
DSP (by log-like)	1 Gaussian	medium	-6.152 $\pm$5.144	6	$\approx$ 33.322 $\pm$5.761
DSP (by log-like)	1 Gaussian	small	-3.861 $\pm$0.480	6	$\approx$ 58.209 $\pm$15.949

Table 19: Results for the $p(\mathbf{Y}|\mathbf{X})$-case of the Stanford-Drone dataset for scenario 1. All Spline models have equal number of knots in y_1 and y_2. The average percent of probability mass covering invalid space ($\mathsf{Pr}(\neg\phi)$) over our test-set is given in percent. It is approximated by sampling 10^6 times per datapoint $\boldsymbol{x}$ in the test-set, computing constraint satisfaction, and then taking the average. After choosing the hyper-parameters, all runs were repeated 10-times and we report mean and standard deviation.

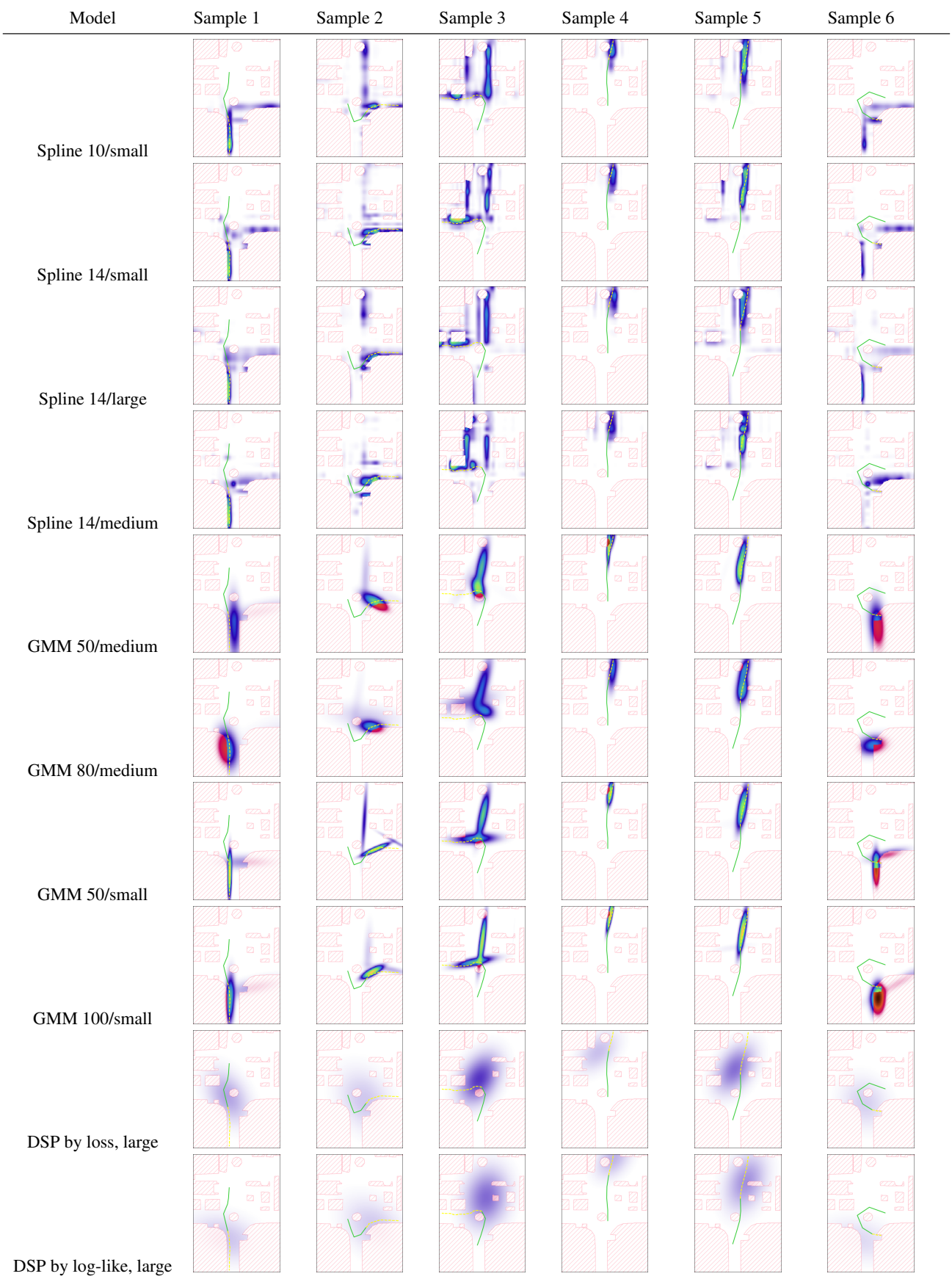

Table 20: Densities for the predictive positions for the $P(\mathbf{Y} \mid \mathbf{X})$ case on the stanford drone dataset for scenario 1. We compare the best 4 spline-models against the best 4 GMM models and the best DSP models both by log-likelihood and loss from 19. The colormap is normalized per sample.

Model	Sample 1	Sample 2	Sample 3	Sample 4	Sample 5	Sample 6
by log-like, large network		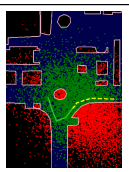	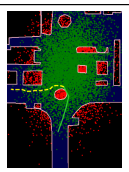			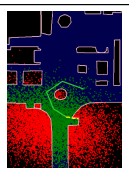
by loss, large network	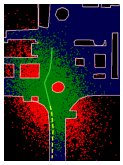				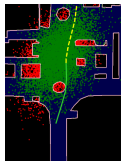	

Table 21: Samples from the Problog-Query representing the Constraints on the Stanford-Drone Dataset. We display the samples and the associated labels that we obtain from DeepSeaProbLog. We show the same samples as displayed in 20.

E.5.3 Scenario 2

We provide further provide results on Image 2 from the Stanford Drone Dataset [Robicquet et al., 2016]. This is a small scenario, with 119 trajectories to start. For the conditional trajectory-prediction problem, we use the same setup is detailed in section E.5 and arrive at 21273 train, 72710 validation, and 62080 test-datapoints.

Model Details

We narrow down our search-space and pick the best-performing configurations from E.5.2 to apply our grid-search on, but discard the large net-size as the dataset is smaller.

`PAL` For the `PAL` models, we do a grid-search over the following parameters:

- **number of mixtures**: 8 and 10
- **number of knots**: 10 and 14 (equal over y_1 and y_2)
- **optimizer** AdamW schedulefree [Defazio et al., 2024] with learning rate: 0.001, 0.0001 and batch-sizes 16, 32 and 128
- **net-sizes**: medium/small

GMM For the conditional GMM-models, we do a grid-search over the following parameters:

- **number of components** K: 4, 32, 50, 100 with full covariances
- **net-sizes**: medium/small
- **optimizer** Adam [Kingma and Ba, 2015b] with learning rates: 0.001, 0.0001 and batch-sizes 16, 32, 128

DSP For the DSP models, we do a grid-search over the following parameters:

- **optimizer** AdaMax [Kingma and Ba, 2015b] with learning rates 0.001, 0.0001 and batch-sizes 16, 32, 128
- **annealing starting-multiplier**: 0.1, 1.0
- **end-multiplier**: 5
- **net-sizes**: medium/small

We use a tanh-scaling of the annealing multiplier with an alpha of $1e-4$ and train with the loss DSP-Loss.

Results

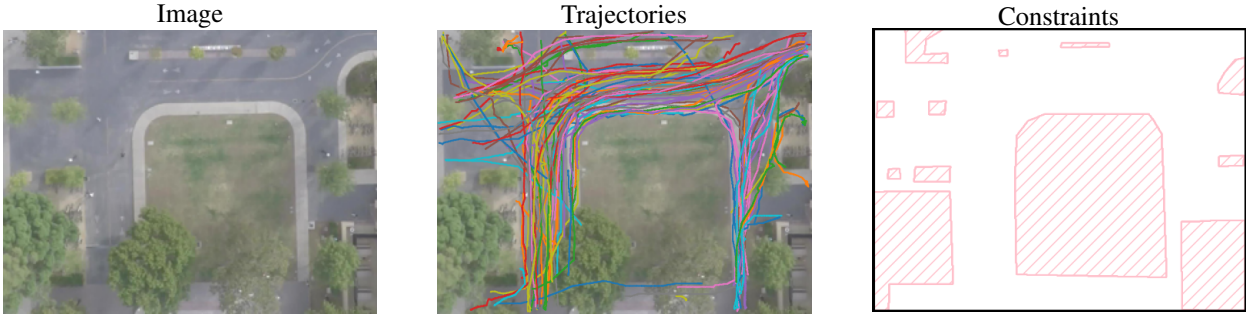

Figure 14: **Our dataset combines challenging constraints with real-world data** on trajectories (middle) and aerial maps (left) taken from Robicquet et al. [2016]. We manually label the data, indicating invalid areas to move to. This is image 2 from the Stanford drone dataset.

type	size dist.	net size	log-like	num. params dist.	$\mathsf{Pr}(\neg\phi)$
NN + PAL	14 knots, 10 mixtures	medium	-2.237 $\pm$0.268	570	**0.000**
NN + PAL	10 knots, 8 mixtures	medium	-2.302 $\pm$0.175	328	**0.000**
NN + PAL	14 knots, 8 mixtures	small	-2.232 $\pm$0.275	456	**0.000**
NN + PAL	10 knots, 10 mixtures	small	**-2.091 $\pm$0.086**	410	**0.000**
NN + GMM	K=100	medium	-2.816 $\pm$0.205	700	$\approx$ 15.435 $\pm$4.099
NN + GMM	K=50	medium	-3.129 $\pm$0.572	350	$\approx$ 14.905 $\pm$3.603
NN + GMM	K=32	medium	-2.714 $\pm$0.228	224	$\approx$ 16.399 $\pm$3.852
NN + GMM	K=4	medium	-2.780 $\pm$0.316	28	$\approx$ 17.271 $\pm$4.785
NN + GMM	K=100	small	-2.423 $\pm$0.193	700	$\approx$ 14.684 $\pm$2.973
NN + GMM	K=50	small	-2.396 $\pm$0.231	350	$\approx$ 15.610 $\pm$3.715
NN + GMM	K=32	small	-2.674 $\pm$0.310	224	$\approx$ 15.390 $\pm$4.273
NN + GMM	K=4	small	-2.650 $\pm$0.281	28	$\approx$ 19.093 $\pm$6.341
DSP by loss	1 Gaussian	medium	-3.611 $\pm$0.287	6	$\approx$ 35.986 $\pm$6.946
DSP by loss	1 Gaussian	small	-30.006 $\pm$76.260	6	$\approx$ 52.929 $\pm$17.107
DSP by log-like	1 Gaussian	medium	-3.611 $\pm$0.287	6	$\approx$ 36.148 $\pm$1.641
DSP by log-like	1 Gaussian	small	-29.967 $\pm$76.274	6	$\approx$ 36.433 $\pm$2.976

Table 22: Results for the $P(Y|X)$-case of the Stanford-Drone dataset for scenario 2. All Spline models have equal number of knots in y_1 and y_2. The average percent of probability mass covering invalid space ($\mathsf{Pr}(\neg\phi)$) over our test-set is given in percent. It is approximated by sampling 10^6 times per datapoint $\boldsymbol{x}$ in the test-set, computing constraint satisfaction, and then taking the average. After choosing the hyper-parameters, all runs were repeated 10-times and we report mean and standard deviation.

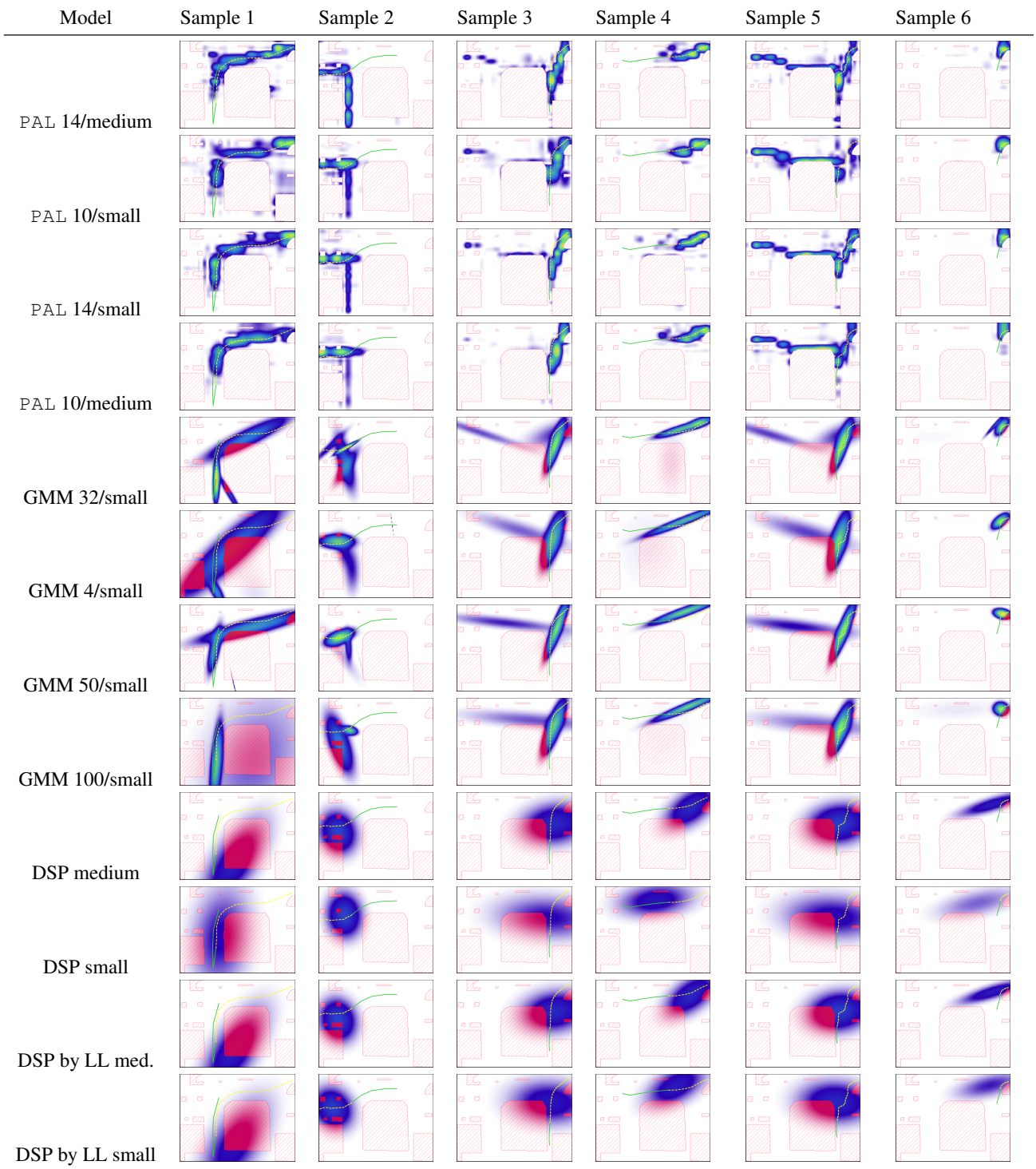

Table 23: Densities for the predictive positions for the $P(\mathbf{Y} \mid \mathbf{X})$ case on the Stanford drone dataset on scenario 2. We compare the best 4 spline models against the best 4 GMM models and the best DSP models both by log-likelihood and loss from 22. Colormap is normalized per sample.

F SAMPLING

We implement sampling through autoregressive inverse-transform sampling using bisection search. In our sampling procedure we assume $\mathbf{Y}$ to be continuous, although it is straightforward to extend this approach to the hybrid case. Autoregressive inverse-transform sampling works through repeatedly applying the inverse-transform technique, conditioning on all the already sampled dimensions and marginalizing out all the subsequent dimensions.

In order to derive our algorithm, we will first focus on sampling the i-th dimension conditioned on our sampled previous dimensions, for which we first need to define the conditional CDF F:

$$
\begin{aligned}
F(z) &= p(Y_i \leq z \mid \mathbf{Y}_{1:(i-1)} = \boldsymbol{y}_{1:(i-1)}) \\
&\propto \int \int_{-\infty}^{z} q(\mathbf{Y}_{i+1:n} = \boldsymbol{y}_{i+1:n}, Y_i = y, \mathbf{Y}_{1:(i-1)} = \boldsymbol{y}_{1:(i-1)}) \cdot \mathbb{1}\{\boldsymbol{y} \models \phi\} \, dy d\boldsymbol{y}_{i+1:n} \\
&= \int \int_{-\infty}^{z} q'(\mathbf{Y}_{i+1:n} = \boldsymbol{y}_{i+1:n}, Y_i = y) \cdot \mathbb{1}\{(y, \boldsymbol{y}_{i+1:n}) \models \phi'\} \, dy d\boldsymbol{y}_{i+1:n} \\
&= \int q'(\mathbf{Y}_{i:n} = \boldsymbol{y}_{i:n}) \cdot \mathbb{1}\{\boldsymbol{y}_{i:n} \models (\phi' \wedge (Y_i \leq z))\} \, d\boldsymbol{y}_{i:n} \\
&= \hat{F}(z)
\end{aligned}
$$

with q' denoting $q[\mathbf{Y}_{1:(i-1)} \mapsto \boldsymbol{y}_{1:(i-1)}]$ and ϕ' denoting $\phi[\mathbf{Y}_{1:(i-1)} \mapsto \boldsymbol{y}_{1:(i-1)}]$.

As we can now deduce $F(z) = \hat{F}(z)/\hat{F}(\infty)$, we have reduced our conditional CDF to our usual weighted model integral, which we can tackle with `GASP!`. As we need the inverse of F for the inverse-transform sampling, we numerically invert the F using bisection search. This leads us to our algorithm:

Algorithm 5 Sample(q, ϕ, ϵ)

Input Polynomial q, Constraint ϕ, Precision ϵ
Output Sample $\boldsymbol{y}$

$\boldsymbol{y}' \leftarrow []$
$n \leftarrow \mathsf{dim}(\mathsf{domain}(q))$
for $i \leftarrow 1$ **to** n **do**
  $q' \leftarrow q[\mathbf{Y}_{1:(i-1)} \mapsto \boldsymbol{y}']$
  $\phi' \leftarrow \phi[\mathbf{Y}_{1:(i-1)} \mapsto \boldsymbol{y}']$
  $f_\infty \leftarrow \texttt{GASP!}(q, \phi')$
  $F(z) = \texttt{GASP!}(q, \phi' \wedge (Y_i \leq z))/f_\infty$
  $lower, upper \leftarrow \mathsf{GlobalBounds(i)}$
  $u \leftarrow \mathsf{sample}(U[0, 1])$
  $y_i \leftarrow \mathsf{BisectionSearch}(F, u, lower, upper, \epsilon)$
  $\boldsymbol{y}' \leftarrow \mathsf{append}(\boldsymbol{y}', y_i)$
end for
return $\boldsymbol{y}'$

In case we are dealing with splines, as we do in the Stanford-Drone Dataset, we already have an expression for the partition function, and therefore the integral over each bin at hand. We can therefore speed up the sampling by deciding on a bin first:

We visualize our results in figure 15. Here we show the drawing of 100 samples applied to Sample 1 from 23 for the model `PAL` 14/medium. It takes around a second to generate a sample, with 15 `GASP!` evaluations per sample. We generate a sample up to an epsilon of 0.1 (in pixel space), which is a sensible value considering that we know that the precision of our ground truth positions is limited by the resolution of our image.

Algorithm 6 BisectionSearch$(f, u, lower, upper, \epsilon)$

Input function $f : \mathbb{R} \to \mathbb{R}$, target u, bounds $(lower, upper)$, precision ϵ
Output Point z, ϵ-close to the generalized left-inverse $F^{-1}(u)$

while $upper - lower > \epsilon$ **do**
  $m \leftarrow \frac{upper+lower}{2}$
  if $f(mid) \leq u$ **then**
    $lower \leftarrow mid$
  else
    $upper \leftarrow mid$
  end if
end while
return $\frac{upper+lower}{2}$

Algorithm 7 SamplePiecewise$(q_{i=1}^m, \phi, I_{i=1}^m, b_{i=1}^m, \epsilon)$

Input Polynomials q, Constraints ϕ, Integrals per bin $I_{i=1}^m$, Bounds $b_{i=1}^m$, Precision ϵ
Output Sample $\boldsymbol{y}$

$j \leftarrow \mathsf{sampleCategorical}(I_{i=1}^m / \mathsf{sum}(I_{i=1}^m))$
$n \leftarrow \mathsf{dim}(\mathsf{domain}(q_1))$
$\phi' \leftarrow \phi \wedge (\bigwedge_{i=1}^n (Y_i \geq \mathsf{lower}(b_j)_i \wedge Y_i \leq \mathsf{upper}(b_j)_i)$
$\boldsymbol{y} \leftarrow \mathsf{Sample}(q_j, \phi', \epsilon)$
return $\boldsymbol{y}$

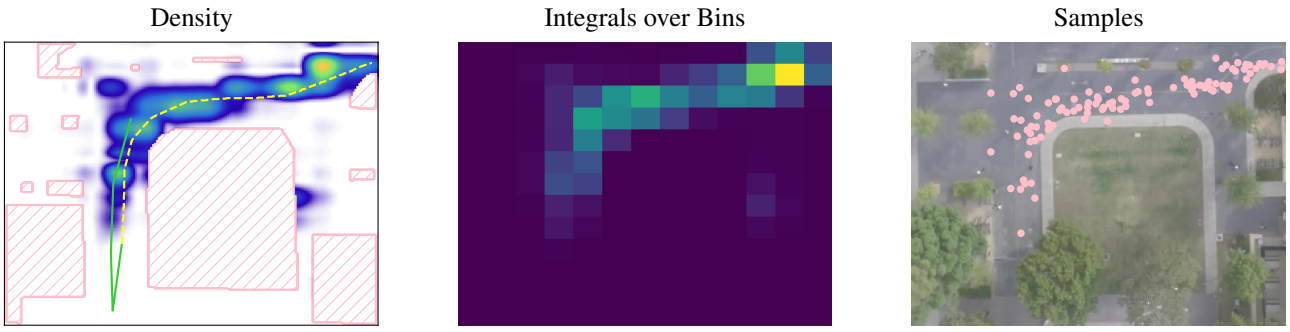

Figure 15: The obtained samples from our sampling procedure applied to Sample 1 from 23 for the model PAL 14/medium. On the left one can see the ground truth density of our spline-based PAL-model, followed by the integral over the bins. On the right, we show the 100 samples drawn by applying algorithm 7.